A global CO₂ flux dataset (2015–2019) inferred from OCO-2 retrievals using the Tan-Tracker inversion system

Zhe Jin[1,3], Xiangjun Tian[2,3,4], Rui Han[1,3], Yu Fu[5], Xin Li[2], Huiqin Mao[6], and Cuihong Chen[6]

[1]International Center for Climate and Environment Sciences, Institute of Atmospheric Physics, Chinese Academy of Sciences, Beijing, 100029, China
[2]National Tibetan Plateau Data Center, Key Laboratory of Tibetan Environment Changes and Land Surface Processes, Institute of Tibetan Plateau Research, Chinese Academy of Sciences, Beijing, 100101, China
[3]College of Earth and Planetary Sciences, University of Chinese Academy of Sciences, Beijing, 100049, China
[4]Collaborative Innovation Center on Forecast and Evaluation of Meteorological Disasters, Nanjing University of Information Science and Technology, Nanjing. 210044, China
[5]Climate Neutrality Research Center, Institute of Atmospheric Physics, Chinese Academy of Sciences, Beijing, 100029, China
[6]Satellite Application Center for Ecology and Environment, Ministry of Ecology and Environment of the People's Republic of China, Beijing, 100094,China

Correspondence to: Xiangjun Tian (tianxj@itpcas.ac.cn), and Xin Li (xinli@itpcas.ac.cn)

Abstract. Accurate assessment of the various sources and sinks of carbon dioxide (CO_2), especially terrestrial ecosystem and ocean fluxes with high uncertainties, is important for understanding of the global carbon cycle, supporting the formulation of climate policies, and projecting future climate change. Satellite retrievals of the column-averaged dry air mole fractions of CO_2 (XCO_2) are being widely used to improve carbon flux estimation due to their broad spatial coverage. However, there is no consensus on the robust estimates of regional fluxes. In this study, we present a global and regional resolved terrestrial ecosystem carbon flux (NEE) and ocean carbon flux dataset for 2015–2019. The dataset was generated using the Tan-Tracker inversion system by assimilating Observing Carbon Observatory 2 (OCO-2) column CO_2 retrievals. The posterior NEE and ocean carbon fluxes were comprehensively validated by comparing posterior simulated CO_2 concentrations with OCO-2 independent retrievals and Total Carbon Column Observing Network (TCCON) measurements. The validation showed that posterior carbon fluxes significantly improved the modelling of atmospheric CO_2 concentrations, with global mean biases of 0.33 ppm against OCO-2 retrievals and 0.12 ppm against TCCON measurements. We described the characteristics of the dataset at global, regional, and Tibetan Plateau scales in terms of the carbon budget, annual and seasonal variations, and spatial distribution. The posterior 5-year annual mean global atmospheric CO_2 growth rate was 5.35 PgC yr⁻¹, which was within the uncertainty of the Global Carbon Budget 2020 estimate (5.49 PgC yr⁻¹). The posterior annual mean NEE and ocean carbon fluxes were –4.07 and –3.33 PgC yr⁻¹, respectively. Regional fluxes were analysed based on TransCom partitioning. All 11 land regions acted as carbon sinks, except for Tropical South America, which was almost neutral. The strongest carbon sinks were located in Boreal Asia, followed by Temperate Asia and North Africa. The entire Tibetan Plateau ecosystem was estimated as a carbon sink, taking up –49.52 TgC yr⁻¹ on average, with the strongest sink occurring in eastern alpine meadows. These results indicate that our dataset captures surface carbon fluxes well and provides insight into the global carbon cycle. The dataset can be accessed at https://doi.org/10.11888/Meteoro.tpdc.271317 (Jin et al., 2021).

1   Introduction

Anthropogenic carbon dioxide (CO_2) emissions are dominant sources for increasing atmospheric CO_2 concentrations. Total emissions are partitioned among the atmosphere, land, and ocean. During the past decade (2010–2019), 31 % and 23 % of emissions were absorbed by the land and ocean, respectively (Friedlingstein et al., 2020). However, there is little agreement on the magnitude and interannual variability of land and ocean fluxes at regional scales (Hauck et al., 2020; Piao et al., 2020; Eldering et al., 2017; Piao et al., 2009). Precise knowledge of the various reservoirs within the carbon cycle is a prerequisite to monitor flux changes and make well-informed projections under future climate change (Zscheischler et al., 2017).

Atmospheric inversions provide important insight into the global carbon cycle through absorbing atmospheric CO_2 observations. Many inversion studies have utilized high-precision *in situ* and flask observations to infer surface CO_2 fluxes (Peters et al., 2007; Chevallier et al., 2010; Lauvaux et al., 2016). Although this is a useful way to quantify carbon fluxes at large scales, estimate uncertainty grows quickly as the scale shrinks due to the lack of observations outside of North America and Europe (Crowell et al., 2019; Byrne et al., 2017; Peylin et al., 2013). To improve spatial coverage and fill observation gaps of *in situ* CO_2 network, column-averaged CO_2 mole fraction (XCO_2) observations from satellites have been extensively applied to flux inversions. The Greenhouse gases Observing SATellite (GOSAT) was the first dedicated greenhouse gas satellite (Yokota et al., 2009), followed by Orbiting Carbon Observatory 2 (OCO-2) (Crisp et al., 2004). Inversions using GOSAT retrievals can significantly reduce the uncertainty of flux estimates in regions where surface CO_2 observations are sparse; however, no agreement is achieved on the estimates of regional fluxes (Chevallier et al., 2014; Basu et al., 2013; Takagi et al., 2011). Compared with GOSAT, OCO-2 has higher spatial resolution, broader spatial coverage, and collects more measurements per day (Eldering et al., 2017). Its higher measurement signal-to-noise ratio allows for higher-precision XCO_2 retrievals, and its higher spatial sampling density facilitates validation using the ground-based Total Carbon Column Observing Network (TCCON) (Liang et al., 2017; Wunch et al., 2017). Based on these characteristics, OCO-2 may provide better constraints on surface CO_2 fluxes inversions (Basu et al., 2018). Chevallier et al. (2019) indicated that large-scale annual fluxes estimated from bias-corrected OCO-2 land retrievals are within the uncertainty of fluxes estimated from the surface network. Villalobos et al. (2020) performed idealized flux inversion experiments over Australia using OCO-2 retrievals and found that the integrated flux uncertainty was greatly reduced and flux inversions at the unusually fine scale yielded useful information on the carbon cycle at continental and finer scales. With the refinement of instrument error characterization, retrieval algorithms, and bias correction procedures, the accuracy and precision of satellite-retrieved XCO_2 have improved significantly (O'dell et al., 2018; Kiel et al., 2019). The effectiveness and potential of these constantly updated satellite retrievals for inferring surface CO_2 fluxes requires further and persistent investigation.

In the global carbon cycle, the response of carbon fluxes in the Tibetan Plateau ecosystems play an important role (Nieberding et al., 2020; Li et al., 2016). The plateau's crucial role is almost entirely due to its height, with an area of 2.5 million km^2 at an average elevation exceeding 4000 m above sea level (Qiu, 2008). The temperature on the Tibetan Plateau has increased by 0.35 °C per decade from 1970 to 2014, at a pace that is about three times the observed rate of global warming,

resulting in significant permafrost thawing and glacier retreat (Yao et al., 2019). These warming-induced environmental issues may enhance the productivity of grasslands and soil respiration, as well as substantial emissions of old CO_2 (Ding et al., 2017;
70   Du et al., 2018). However, there are many uncertainties in the Tibetan Plateau carbon cycle under climate change, which are further amplified by human activities (Chen et al., 2013; Piao et al., 2019). Previous studies on Tibetan Plateau carbon fluxes mainly relied on ground-based measurements; the application of satellite data is promising to compensate for ground-based findings and reveal new information about the carbon cycle.

In this study, we used the Tan-Tracker inversion system (Tian et al., 2014a, 2014b) to generate a global dataset containing
75   terrestrial ecosystem carbon fluxes and ocean carbon fluxes from 2015 to 2019 by assimilating OCO-2 XCO_2 retrievals. The Tan-Tracker inversion system adopts a dual-pass inversion strategy and the nonlinear least squares four-dimensional variational data assimilation (NLS-4DVar) method (Tian and Feng, 2015; Tian et al., 2018). The dual-pass strategy well distinguishes simulated CO_2 errors from uncertainties in both the initial CO_2 concentrations and carbon fluxes. The NLS-4DVar method comprising a fast localization module (Zhang and Tian, 2018) is able to assimilate large amounts of
80   observations within an inversion window and obtain high accuracy inversion with low computational complexity. Compared with previous versions of Tan-Tracker, we improved the dual-pass strategy of Tian et al. (2014a), embedded the upgraded ensemble update scheme (Tian et al., 2020) to guarantee the system's stable operation, and updated the GEOS-Chem transport model (Nassar et al., 2010) to v12.9.3 (http://www.geos-chem.org). In the dataset, we present optimized global daily gridded terrestrial ecosystem and ocean carbon fluxes with a spatial resolution of 2° latitude × 2.5° longitude. Corresponding fluxes
85   from other sectors are also available (e.g., fossil fuel emissions, biomass burning emissions) to infer the global carbon budget. Besides, global model-simulated CO_2 concentrations forced by optimized fluxes are provided. The optimized fluxes were comprehensively validated against independent OCO-2 retrievals and TCCON XCO_2 observations. Data users can calculate the preferred carbon fluxes at a global or regional scale according to their needs for further analysis or comparison with other sources of flux information.

90   This paper is organized as follows: Sect. 2 describes the methods and data employed; Sect. 3 and 4 describe the dataset and its characteristics, respectively; Sect. 5 evaluates the posterior fluxes against OCO-2 retrievals and TCCON observations; Sect. 6 discusses the strengths and limitations of the method and dataset, as well as future developments; Sect. 7 introduces the data availability; the conclusion is presented in Sect. 8.

2 Methods and Data

95   ### 2.1 Tan-Tracker inversion system

Figure 1 shows the frame of the Tan-Tracker inversion system. The fluxes to be optimized are terrestrial ecosystem carbon fluxes (i.e., net ecosystem exchange, NEE) and atmosphere-ocean carbon exchange, whereas other fluxes (e.g., fossil fuel emissions and biomass burning emissions) are assumed to have no errors. This assumption is commonly adopted in global flux inversion systems (Peters et al., 2007; Nassar et al., 2011; Crowell et al., 2019; Jiang et al., 2021). The core of Tan-Tracker is

a novel dual-pass inversion strategy with modifications to Tian et al. (2014a, 2014b) and the NLS-4DVar method (Tian and Feng, 2015; Tian et al., 2018). This dual-pass strategy performs assimilations twice within an inversion window. First, the CO_2 assimilation pass is performed using the prior fluxes within a short time (5 days) to obtain the optimized initial CO_2 concentrations; then, the flux assimilation pass is performed using the optimized initial CO_2 concentrations within a longer time (14 days) to obtain the optimized fluxes. This strategy well distinguishes the CO_2 simulation deviation caused by errors from initial CO_2 concentrations and carbon fluxes. When assimilation of the current inversion window is complete, the prior initial CO_2 concentrations before assimilation and the posterior fluxes are used to actuate the atmospheric chemistry transport model, which simulates the period from the initial moment of the current window to the initial moment of the next window to obtain the initial CO_2 concentrations of the next window. Then, the previous steps are repeated, performing cyclic data assimilation.

The Tan-Tracker optimization procedure is realized using the NLS-4DVar method (Tian and Feng, 2015; Tian et al., 2018). The optimization minimizes the following cost function:

$$J(x) = \frac{1}{2}(x - x_a)^{\mathrm{T}}(B^{prior})^{-1}(x - x_a) + \frac{1}{2}(y - h(x))^{\mathrm{T}}R^{-1}(y - h(x)). \tag{1}$$

where x is the state variable (i.e., the variable to be optimized) and x_a is the prior state variable, B^{prior} is the prior error covariance matrix, y is the observed CO_2 concentrations, $h(\cdot)$ is the observation operator, and R is the observation error covariance matrix. The state variable of the CO_2 assimilation pass is CO_2 concentrations, whereas that of the flux assimilation pass is the scaling factor, that is:

$$F_{i,j}^{post} = \lambda_{i,j}^{post} \times F_{i,j}^{prior}. \tag{2}$$

where $F_{i,j}^{post}$ is the posterior carbon flux, $\lambda_{i,j}^{post}$ is the posterior scaling factor, and $F_{i,j}^{prior}$ is the prior carbon flux, $i = 1,2, \dots, I$, $j = 1,2, \dots, J$, and I and J denote the numbers of grids in longitude and latitude, respectively. Both of fluxes and scaling factors are gridded variables.

The Tan-Tracker inversion system uses the global three-dimensional (3D) atmospheric chemistry transport model GEOS-Chem to simulate CO_2 concentrations in the atmosphere (Suntharalingam et al., 2004; Nassar et al., 2010, 2013). The spatial resolution of GEOS-Chem is 2° latitude × 2.5° longitude, with 47 layers in the vertical direction. The model is driven by the various carbon fluxes, initial CO_2 concentrations, and Modern-Era Retrospective analysis for Research and Applications 2 (MERRA-2) meteorological data provided by the Goddard Earth Observing System (GEOS) of the National Aeronautics and Space Administration (NASA) Global Modeling and Assimilation Office (Gelaro et al., 2017). The observations assimilated are OCO-2 column CO_2 (XCO_2) retrievals (O'dell et al., 2012; O'dell et al., 2018). In this study, we optimized the global NEE and atmosphere-ocean carbon fluxes during 2015–2019 using the Tan-Tracker inversion system. The configurations of Tan-Tracker are described in Table 1.
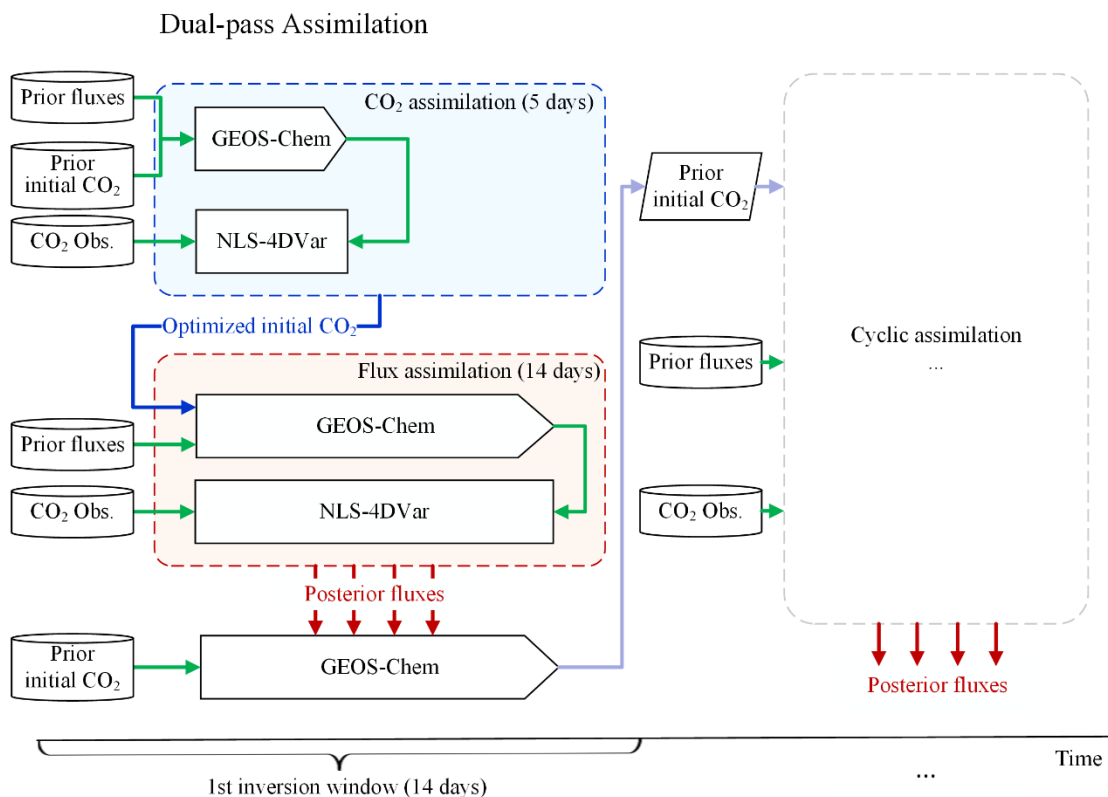
Figure 1. Flowchart of the Tan-Tracker inversion system.

Table 1. Configurations of the Tan-Tracker inversion system.

	System setup	Configuration	Reference
Inversion setup	Inversion strategy	Dual pass	Tian et al. (2014a); Tian et al. (2014b); Han and Tian (2019)
	Optimized fluxes	Terrestrial ecosystem carbon flux (NEE) and atmosphere-ocean carbon exchange	Peters et al. (2007); Jiang et al. (2021)
	Assimilated data	OCO-2 XCO_2 retrievals	O'dell et al. (2012); O'dell et al. (2018)
	Inversion method	NLS-4DVar method	Tian and Feng (2015); Tian et al. (2018)
	State variable	CO_2 concentration for CO_2 pass; scale factor for flux pass	–
	Assimilation window	5 days for CO_2 pass; 14 days for flux pass	–

Transport model	GEOS-Chem	Version 12.9.3	Suntharalingam et al. (2004); Nassar et al. (2010); Nassar et al. (2013)
	Spatial scale	Global	–
	Spatial resolution	2° latitude × 2.5° longitude, 47 vertical levels	–
	Meteorological forcing	MERRA-2	(Gelaro et al., 2017)

2.2 Prior CO_2 fluxes

The various carbon fluxes required to drive GEOS-Chem to simulate atmospheric CO_2 concentrations included NEE, ocean
135 carbon fluxes, fossil fuel emissions, biomass burning emissions, ship emissions, aviation emissions, biofuel burning emissions,
and chemical production of CO_2 (Table 2). The 3D chemical source of CO_2 includes the oxidation of CO, CH_4 and other carbon
gases. As fossil fuel emission and biospheric inventories used to count CO_2 precursor species (CO, CH_4 and other carbon gases)
as direct CO_2 emissions at the surface, whereas real chemical production of CO_2 from these species occurs at different times
and locations from emission, model implementation of CO_2 chemical production requires adjustments to these surface emission
140 inventories (Nassar et al., 2010).

The optimized fluxes were NEE and ocean-atmosphere exchange. The prior NEE was obatined from CarbonTracker
CT2019B (Jacobson et al., 2020), which provides data from January 2000 until March 2019, with a spatial resolution of 1° ×
1° and temporal resolution of 3 h. CarbonTracker is a CO_2 measurement and modeling system developed by the National
Oceanic and Atmospheric Administration (NOAA) that tracks CO_2 sources and sinks worldwide. CarbonTracker uses ground-
145 based atmospheric CO_2 observations from a host of collaborators and simulates atmospheric transport to estimate surface CO_2
fluxes (Peters et al., 2007). The prior ocean carbon fluxes were obtained from Takahashi et al. (2009), which contains monthly
data from 2000 to 2013 with a horizontal resolution of 4° × 5°. As the original ocean flux dataset does not cover the simulation
period of this study, we used NOAA Marine Boundary Layer (MBL) Reference data of CO_2
(https://www.esrl.noaa.gov/gmd/ccgg/mbl/index.html, last accessed: 26 April 2021) to extend the ocean flux to 2018. NOAA
150 MBL Reference is a data product derived directly from measurements of weekly air samples collected by the Cooperative Air
Sampling Network; the zonally-averaged MBL reference can be used to identify large-scale trends in atmospheric greenhouse
gases (Conway et al., 1994). According to the correlation of MBL CO_2 concentration and ocean carbon fluxes described in
Takahashi et al. (2009), we constructed the ocean fluxes for 2014–2018 using corresponding MBL data. Due to a lack and
deficiency of data for 2019, prior NEE and ocean carbon fluxes for 2018 were used as 2019 prior estimates.

155 **Table 2. Summary of inventories used for the GEOS-Chem CO_2 simulation in this work.**

Flux Type	Inventory name/ abbreviation	Description	References

Fossil fuel emissions	ODIAC	$1° \times 1°$ monthly global emissions	Oda and Maksyutov (2011); Oda et al. (2018b)
Net ecosystem exchange (NEE)	CarbonTracker CT2019B	$1° \times 1°$ 3-hourly averaged data	Jacobson et al. (2020)
Ocean carbon fluxes	Takahashi et al. (2009)	$4° \times 5°$ climatology of monthly ocean-atmosphere CO_2 fluxes	Takahashi et al. (2009)
Biomass burning emissions	GFED v4	$0.25° \times 0.25°$ monthly data scaled with daily factors	Van Der Werf et al. (2017); Randerson et al. (2017)
Ship emissions	CEDS	$0.5° \times 0.5°$ monthly ship emissions	Hoesly et al. (2018)
Aircraft emissions	AEIC	$1° \times 1°$ with 47 vertical levels, aviation fuel burning from AEIC scaled with global annual CO_2 emission totals calculated from IEA	Olsen et al. (2013); Simone et al. (2013)
Biofuel burning emissions	Yevich & Logan	$1° \times 1°$ annual inventory of biofuel CO_2 emissions for 1985 and scaled to 1995	Yevich and Logan (2003)
Chemical source	GEOS-Chem CO_2 chemical source	Chemical production of CO_2 based on CO loss rates from GEOS-Chem $4° \times 5°$ simulations	Nassar et al. (2010)

2.3 OCO-2 column CO_2 observations

The OCO-2 Level 2 Lite (v9r) carbon dioxide column-averaged dry-air mole fraction (XCO_2) products retrieved by the Atmospheric Carbon Observations from Space (ACOS) algorithm (Connor et al., 2008) were used in this study (O'dell et al., 2012; O'dell et al., 2018). The OCO-2 satellite carries high-resolution spectrometers that return high-precision measurements 160 of reflected sunlight received within the CO_2 and O_2 bands in the short-wave infrared spectrum (Crisp et al., 2012). The OCO-2 spacecraft flies in a 705-km-altitude sun-synchronous orbit, with a 16-day (233 orbits) ground track repeat cycle. OCO-2 has a footprint of $1.29 \times 2.25 \text{ km}^2$ at nadir mode and acquires eight cross-track footprints, creating a swath width of 10.3 km. After filtering and bias correction, the OCO-2 XCO_2 retrievals (v7) agree well when aggregated around and coincident with ground-based TCCON data in nadir, glint, and target observation modes, with absolute median differences of < 0.4 ppm and root-165 mean-square differences of < 1.5 ppm (Wunch et al., 2017). O'dell et al. (2018) demonstrated that OCO-2 retrieval error variance with respect to TCCON was reduced by 20 % over land and 40 % over ocean between versions 7 and 8, with improved nadir and glint observation consistency over land.

Considering the quality and large amount of OCO-2 XCO_2 observations, we performed quality control and observation thinning to filter out some retrievals (Han and Tian, 2019). The observation preprocessing procedure included three steps. In

170 the first step, observations were filtered according to the xco2_quality_flag and xco2_uncertainty parameters provided by the OCO-2 Lite product. xco2_quality_flag = 0 denotes the retrieval quality is good whereas xco2_quality_flag = 1 denotes the quality is bad. We selected only observations with xco2_quality_flag = 0. The xco2_uncertainty parameter represents the posterior uncertainty of XCO_2 retrieval, and observations with xco2_uncertainty > 1.5 ppm were filtered out. In the second step, differences between OCO-2 XCO_2 and corresponding model-simulated XCO_2 were considered. The observation was

175 discarded when the absolute difference exceeded 2 ppm, or the difference was beyond the range of two standard deviations above or below the daily mean difference. In the third step, if the number of observations remaining after the first two filtering steps exceeded 20,000, then the observation too close to the previous one was eliminated to maintain a number of observations around 20,000. Figure 2 shows the OCO-2 observations in the first inversion window before and after quality control and thinning. After the preprocessing procedure, extremely large and small observations were excluded. Observations over the

180 Antarctic were generally discarded due to poor quality (xco2_quality_flag = 1), perhaps because of a small solar altitude angle (O'dell et al., 2018).
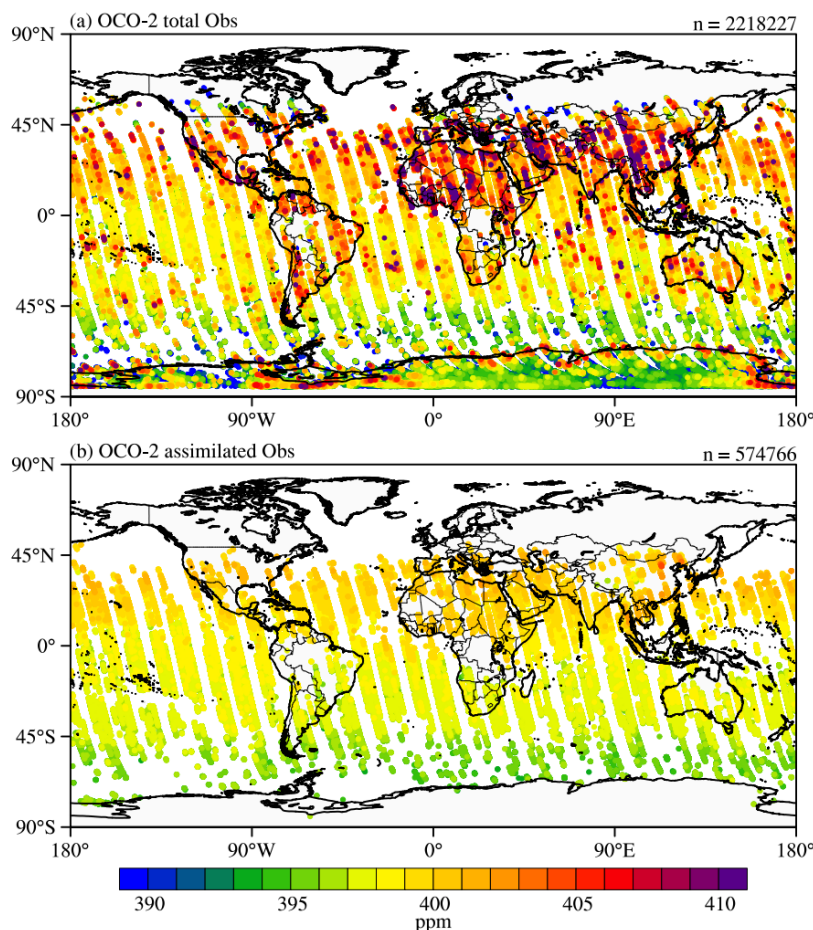
Figure 2. Spatial distributions of (a) all OCO-2 XCO₂ observations and (b) observations after quality control and thinning in the first inversion window (2015.1.1–2015.1.14).

185   During the optimization procedure, simulated and satellite observations were used to calculate the second term in Eq. (1). The xco2_uncertainty parameter provided by the OCO-2 Level 2 Lite product was used to construct the observation error covariance matrix $\mathbf{R}$; observation errors were assumed to be independent of each other. We used an observation operator to project the model-simulated 3D atmospheric CO_2 concentration to the satellite column-averaged concentration. According to Connor et al. (2008), the observation operator is expressed as follows:

190     $$XCO_2^m = XCO_2^a + \boldsymbol{h}^T\mathbf{A}(\boldsymbol{x} - \boldsymbol{x}_a). \tag{3}$$

where XCO_2^m is the model simulated column concentration, XCO_2^a is the prior column concentration, $\boldsymbol{h}$ is the pressure weighting function, $\mathbf{A}$ is the averaging kernel matrix, $\boldsymbol{x}$ is the modeled CO_2 profile, and $\boldsymbol{x}_a$ is the prior profile.

2.4 Uncertainty quantification and ensemble update

As a hybrid method based on 4DVar and the ensemble Kalman filter (EnKF), the NLS-4DVar method applies an ensemble to
195   approximate the prior error covariance matrix (Tian et al., 2018) as follows:

$$\mathbf{B}^{prior} = \frac{\left(\mathbf{P}_x^{prior}\right)\left(\mathbf{P}_x^{prior}\right)^T}{N-1}. \tag{4}$$

where $\mathbf{P}_x^{prior} = (\boldsymbol{x}_1', \boldsymbol{x}_2', \dots, \boldsymbol{x}_N')$ is an ensemble of prior perturbations, $\boldsymbol{x}_j' = \boldsymbol{x}_j - \boldsymbol{x}_a, j = 1,2, \dots, N$, $\boldsymbol{x}_j$ is the jth perturbation, and N is the number of prior perturbations. According to Evensen (2009), the ensemble of posterior perturbations after assimilation is calculated as follows:

200     $$\mathbf{P}_x^{post} = \mathbf{P}_x^{prior}\mathbf{V}_2\sqrt{\mathbf{I} - \boldsymbol{\Sigma}_2^T\boldsymbol{\Sigma}_2}\Phi^T, \tag{5}$$

where

$$\mathbf{U}_2\boldsymbol{\Sigma}_2\mathbf{V}_2^T = \mathbf{X}_2, \tag{6}$$

$$\mathbf{X}_2 = \boldsymbol{\Lambda}^{-1/2}\mathbf{Z}^T\mathbf{P}_y, \tag{7}$$

$$\mathbf{Z}\boldsymbol{\Lambda}^{-1}\mathbf{Z}^T = \left[\left(\mathbf{P}_y\right)\left(\mathbf{P}_y\right)^T + (N-1)\mathbf{R}\right]^{-1}. \tag{8}$$

205   and Φ is a random orthogonal matrix, $\mathbf{P}_y = h\left(\mathbf{P}_x^{prior}\right) - h(\boldsymbol{x}_a)$. Then, the prior ($\mathbf{B}^{prior}$) and posterior ($\mathbf{B}^{post}$) error covariance matrices can be calculated using $\mathbf{P}_x^{prior}$ and $\mathbf{P}_x^{post}$, respectively, according to Eq. (4). $\mathbf{B}^{prior}$ and $\mathbf{B}^{post}$ represent the prior and posterior uncertainties of scaling factors, respectively. In the flux assimilation pass, the prior perturbations of the scaling factor in the first inversion window were obtained through historical sampling, and prior perturbations in the following windows were generated through ensemble updating. Compared with previous versions (Tian et al., 2014a, 2014b), the current Tan-
210   Tracker system adopts an upgraded ensemble update method that well maintains the ensemble dispersion during cyclic assimilation (Tian et al., 2020). The new ensemble update equation is as follows:

$$\mathbf{P}_{x,r+1}^{prior} = \mathbf{P}_{x,r}^{prior}\mathbf{V}_2\Phi^T. \tag{9}$$

where $\mathbf{P}_{x,r+1}^{prior}$ is the prior perturbations of the $(r + 1)$th window and $\mathbf{P}_{x,r}^{prior}$ is the prior perturbations of the rth window.

After obtaining the prior and posterior uncertainties of the scaling factors, the prior and posterior total flux uncertainties

215 (σ_{total}^{prior} and σ_{total}^{post}) can be calculated according to the correlation between fluxes and scaling factors as follows (Niwa and Fujii, 2020):

$$\sigma_{total}^{prior} = \sqrt{(\boldsymbol{F}^{prior})^{\mathrm{T}}\mathbf{B}^{prior}(\boldsymbol{F}^{prior})}, \tag{10}$$

$$\sigma_{total}^{post} = \sqrt{(\boldsymbol{F}^{prior})^{\mathrm{T}}\mathbf{B}^{post}(\boldsymbol{F}^{prior})}. \tag{11}$$

where we assume that the flux uncertainties are time independent.

220 The uncertainty reduction (UR) rate is an important indicator of inversion system performance. Following Deng et al. (2007), the UR is defined as follows:

$$\mathrm{UR} = \left(1 - \frac{\sigma_{total}^{post}}{\sigma_{total}^{prior}}\right) \times 100\ \%. \tag{12}$$

The magnitudes of the UR rates indicate the degree to which the final inverted fluxes are constrained by atmospheric CO_2 observations.

2.5 Evaluation of posterior fluxes

Generally, it is impossible to directly verify the posterior fluxes due to the lack of flux observations. Instead, we compared the simulated CO_2 concentrations driven by posterior fluxes with CO_2 observations to achieve indirect verification (e.g., Wang et al. (2019); Wu et al. (2020); Liu et al. (2021)). The evaluation of posterior fluxes consists of two parts. First, the simulated CO_2 concentrations were compared with unassimilated OCO-2 XCO_2 retrievals, that is, independent observations. Second, the

230 simulated CO_2 concentrations were validated by comparisons with TCCON XCO_2 observations. TCCON is a network of ground-based Fourier Transform Spectrometers that record direct solar spectra in the near-infrared spectral region. From these spectra, accurate and precise column-averaged CO_2 abundances are retrieved and reported (Wunch et al., 2011). In this study, we used GGG2014 version data from 30 TCCON sites (Wunch et al., 2015); the site locations are shown in Fig. 3.

To statistically evaluate the inversion results, we calculated four statistics: the root mean square error (RMSE), mean bias

235 (BIAS), mean absolute error (MAE), and correlation coefficient (CORR). These four statistics represent the bias, error variance, and linear correlation between the simulated and observed CO_2 concentrations, and are formulated as follows:

$$\mathrm{RMSE} = \sqrt{\frac{1}{M}\sum_{j=1}^{M}\left(h(x)_j - y_j\right)^2}\ ; \tag{13}$$

$$\mathrm{BIAS} = \frac{1}{M}\sum_{j=1}^{M}\left(h(x)_j - y_j\right); \tag{14}$$

$$\mathrm{MAE} = \frac{1}{M}\sum_{j=1}^{M}\left|h(x)_j - y_j\right|; \tag{15}$$

240 $$\mathrm{CORR} = \frac{\sum_{j=1}^{M}(h(x)_j - \overline{h(x)})(y_j - \bar{y})}{\sqrt{\sum_{j=1}^{M}(h(x)_j - \overline{h(x)})^2}\sqrt{\sum_{j=1}^{M}(y_j - \bar{y})^2}}. \tag{16}$$

where $h(x)_j$ and y_j are the jth simulated observation and real observation, respectively. M is the number of observations and the overbar denotes the average.
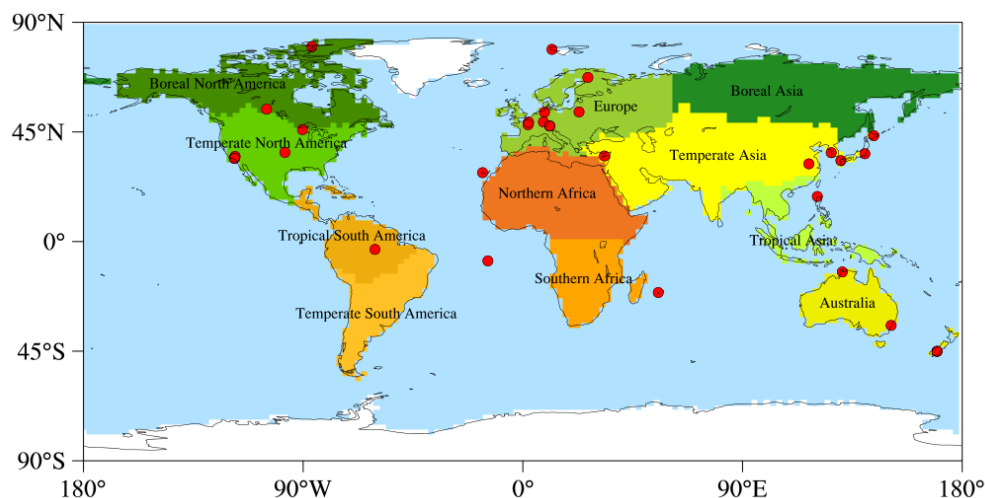
Figure 3. Distribution of 30 TCCON sites used for validation in this study (red circles). Shaded areas indicate the 11 TansCom land regions.

3 Dataset description

Here we present a global gridded dataset containing various carbon fluxes and simulated CO_2 concentrations from 2015 to 2019 (inclusive). The posterior NEE and ocean carbon fluxes were generated using the Tan-Tracker inversion system inferred from OCO-2 XCO_2 retrievals. Apart from these two optimized fluxes, all other emissions listed in Table 2 plus net carbon fluxes are included in the flux files. The global gridded fluxes are daily with a resolution of 2° latitude × 2.5° longitude at 47 vertical levels. The vertical layers are set using the hybrid sigma-pressure grid from GEOS-Chem (http://wiki.seas.harvard.edu/geos-chem/index.php/GEOS-Chem_vertical_grids, last accessed: 14 May 2021). The fluxes are distributed in 47 layers due to the presence of aircraft emissions and chemical sources; the remaining fluxes are surface fluxes. The GEOS-Chem simulated instantaneous CO_2 concentrations actuated by posterior NEE and ocean fluxes were generated every 3 h, at the same spatial resolution as the fluxes. The surface pressure and pressure at each vertical level are provided in the concentration files. The aggregated global annual and monthly fluxes with corresponding uncertainties are provided in tabular format. Users can aggregate the gridded fluxes on their preferred regions and compare the results with other available datasets. The characteristics of the dataset are described in Sect. 4.

4 Characteristics of the dataset

4.1 Global fluxes

4.1.1 Global carbon budget

The annual atmospheric CO_2 growth rate (AGR) is the net difference between total CO_2 emissions and uptake over land and ocean (Jiang et al., 2021). Table 3 presents the annual and annual mean AGR during 2015–2019 estimated from prior and posterior fluxes in this study. For comparison, the AGRs from Global Carbon Budget 2020 (GCB2020; Friedlingstein et al., 2020), CarbonTracker CT2019B (Jacobson et al., 2020), and Jena CarboScope (JCS; Rödenbeck, 2005) (http://www.bgc-jena.mpg.de/CarboScope/?ID=s, last accessed: 26 May 2021) are also included. The AGR of GCB2020 was estimated directly from atmospheric CO_2 concentration measurements, which are provided by the NOAA Earth System Research Laboratory (ESRL; https://www.esrl.noaa.gov/gmd/ccgg/ggrn.php, last accessed: 23 April 2021); it can be considered a true value. The uncertainty of the GCB2020 AGR is around 0.2 PgC yr^{-1}. CT2019B does not contain complete data for 2019; therefore, we have omitted the 2019 annual and annual mean estimates of CT2019B data. JCS provides estimates of surface-atmosphere CO_2 exchange based on atmospheric measurements using atmospheric transport inversion. In this study, we used version s10oc_v2020 of the JCS product. Table 3 shows that prior AGR evaluations were generally greater than those of GCB2020, except for 2018, contributing to a positive annual mean deviation of 0.43 PgC yr^{-1}, mainly due to prior results for 2016 and 2017, which were 0.61 and 1.14 PgC yr^{-1}, respectively. The positive sign of the deviation indicates that prior carbon sources were overestimated, or sinks were underestimated. After absorbing the satellite observations, the posterior AGR weakened every year, with an annual mean of 5.33 PgC yr^{-1}, which was within the uncertainty range of the GCB2020 estimate (5.49 PgC yr^{-1}). The AGRs of CT2019B were generally smaller than those of GCB2020. A comparison of the AGR of CT2019B and GCB2020 throughout 2015–2018 showed a negative deviation of 0.12 PgC yr^{-1}. The AGRs of JCS during 2015–2017 were quite close to the GCB2020 evaluations. The largest deviation in the JCS data occurred in 2019, with a positive deviation of 0.4 PgC yr^{-1} compared with GCB2020. Overall, posterior AGRs were clearly refined compared to the prior, indicating the effectiveness of the flux inversions. Notably, although the annual mean result is comparatively accurate, the annual AGRs still require improvement, which imposes higher requirements on inversion systems.

Table 3. Annual and annual mean global atmospheric CO_2 growth rates (AGRs) during 2015–2019 estimated in this study and in three flux products: GCB 2020, CT2019B, and JCS.

	Atmospheric CO_2 growth rate (PgC yr^{-1})				
	Prior	Posterior	GCB2020	CT2019B	JCS
2015	6.71	5.81	6.28	5.94	6.26
2016	6.71	6.11	6.07	6.24	5.98
2017	5.75	4.98	4.58	4.46	4.55
2018	5.02	4.38	5.09	4.87	4.81

| 2019 | 5.51 | 5.49 | 5.43 | – | 5.83 |
| Annual mean | 5.94 | 5.35 | 5.49 | – | 5.49 |

285 Figure 4 presents the interannual variations and corresponding uncertainties of global NEE and ocean carbon fluxes from prior and posterior estimates as well as GCB2020, CT2019B, and JCS. It should be noted that JCS products contain only the net biosphere exchange (NBE), which is the sum of NEE and biomass burning emissions; therefore, to obtain the NEE of JCS, we subtracted the biomass burning emissions used in this study, such that JCS NEE data represent NBE minus GFED4 v4. The annual mean prior NEE was -3.53 PgC yr^{-1}. Posterior NEE were consistently stronger than prior NEE, varying from $-$

290 3.17 PgC yr^{-1} in 2016 to -4.73 PgC yr^{-1} in 2018, with an annual mean of -4.07 PgC yr^{-1}. The enhancements were obvious during 2015–2018, exceeding 0.5 PgC yr^{-1}. Posterior NEE were generally greater than GCB2020 except for 2016; the largest discrepancy occurred in 2015. However, posterior and GCB2020 estimates of NEE were comparable considering their uncertainties. JCS NEE were basically greater than those of GCB2020, except for 2016, but generally weaker than the posterior ones.

295 For the ocean fluxes, differences between the posterior and prior sinks were moderate during 2015–2019, within 0.15 PgC yr^{-1}. The posterior sinks were strengthened in 2015, 2017, and 2018, and weakened in 2016 and 2019. The posterior ocean sink had an annual value of -3.33 PgC yr^{-1}, slightly stronger than the prior value of -3.29 PgC yr^{-1}. The ocean formed a sink for CO_2 because the gas is highly soluble in seawater, a property that is critical to the ocean's ability to absorb atmospheric CO_2 (Mckinley et al., 2017). During the past two decades, sufficient evidence has been gathered to support the conclusion that

300 the global integrated ocean carbon sink has grown as atmospheric carbon content increases (Khatiwala et al., 2013; Watson et al., 2020). Posterior ocean sinks showed an increasing trend, especially from 2015 to 2018. The GCB2020 ocean flux estimates were quite stable, with an annual mean of -2.60 PgC yr^{-1} and standard deviation of 0.06 PgC yr^{-1}. Posterior ocean sinks were universally greater than the GCB2020 estimates, with the largest deviation occurring in 2018 (1.08 PgC yr^{-1}). Posterior ocean fluxes were more consistent with the CT2019B estimates; both were stronger than the GCB2020 estimates, and those of

305 CT2019B were even stronger than the posterior fluxes. Compared with the posterior and CT2019B results, JCS had smaller ocean sinks and better coherence with GCB2020.
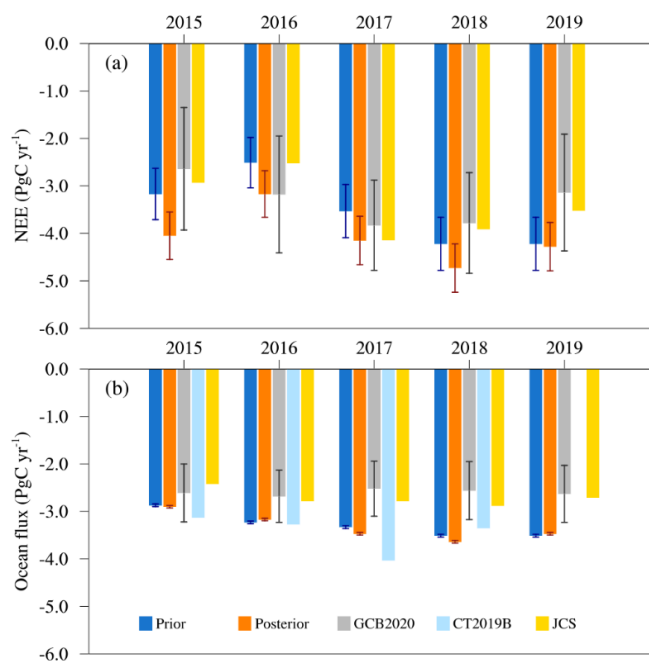
Figure 4. Interannual variations and corresponding uncertainties of global (a) NEE and (b) ocean carbon fluxes from prior and posterior estimates in this study, as well as GCB2020, CT2019B, and JCS products during 2015–2019. Since prior NEE data were obtained from CT2019B, we omitted CT2019B in (a).

Combining the NEE and ocean fluxes, the total posterior annual mean sink was –7.40 PgC yr^{-1}, which is strengthened compared to the prior estimate of –6.82 PgC yr^{-1}, and contributed to a decrease in net carbon emissions that was consistent with the aforementioned AGR estimates. Notably, CO_2 emissions and uptake were classified differently among different inversion systems and GCB2020, preventing NEE and ocean flux estimates from being perfectly equivalent. GCB2020 contains fossil CO_2 emissions, land-use change emissions, and terrestrial and ocean CO_2 sinks. CT2019B includes fossil CO_2 emissions, biomass burning emissions, and terrestrial and ocean CO_2 sinks. In this study, apart from the above mentioned sources and sinks, we additionally considered emissions from shipping, aviation, biofuel burning, and chemical production from CO oxidation (Table 2), providing a more comprehensive consideration of the global carbon cycle. Table A1 shows the annual CO_2 emissions and uptake from all considered sectors. The uncertainties of carbon emissions other than NEE and ocean fluxes are unclear and therefore omitted, but these uncertainties actually exist and should be well described. Both the improvements of inversion methods and accompanying emissions estimates are necessary to obtain more accurate NEE and ocean carbon fluxes.

4.1.2 Seasonal cycle

Figure 5 shows the seasonal cycle and corresponding uncertainties of global NEE and ocean carbon fluxes from prior and posterior estimates during 2015–2019. For NEE, the terrestrial ecosystem emitted CO_2 in winter (December to February) and autumn (September to November), and taken up CO_2 in spring (March to May) and summer (June to August). The prior annual

NEE means for winter, spring, summer, and autumn were 1.74, –0.31, –6.66, and 1.70 PgC, respectively. After inversion, the corresponding posterior fluxes were 1.41, –0.55, –6.32, and 1.39 PgC, respectively. The magnitudes of posterior fluxes in winter, summer, and autumn decreased by 19 %, 5 %, and 18 %, respectively, whereas the magnitude in spring increased by

330   79%, which was the most obvious flux modification. Overall, the annual net sink of terrestrial ecosystems increased. The CO_2 emissions in winter and autumn were roughly equivalent. The largest emissions occurred in October or November, and the posterior range was 0.72 PgC in 2018 to 1.16 PgC in 2015. The net terrestrial ecosystem sinks mainly owed to the large uptake in summer. The largest uptake occurred in July, up to -2.62 ± 0.07 PgC in posterior estimates. Spring uptake was much smaller than in summer, and the posterior estimate in 2016 was nearly neutral (–0.04 PgC).

335   Unlike terrestrial ecosystems, the ocean acted as a carbon sink year-around. The prior annual mean ocean uptake values for winter, spring, summer, and autumn were –0.99, –0.86, –0.68, and –0.77 PgC, respectively. The inversion modifications were not significant, generating posterior estimates of –1.01, –0.89, –0.69, and –0.75 PgC, respectively. The largest and smallest uptakes occurred in winter and summer, respectively. Seasonal changes in the ocean flux field are attributed to the combined effects of seasonal changes in water temperature, biological utilization of CO_2, water mixing, and wind speeds

340   (Takahashi et al., 2002).
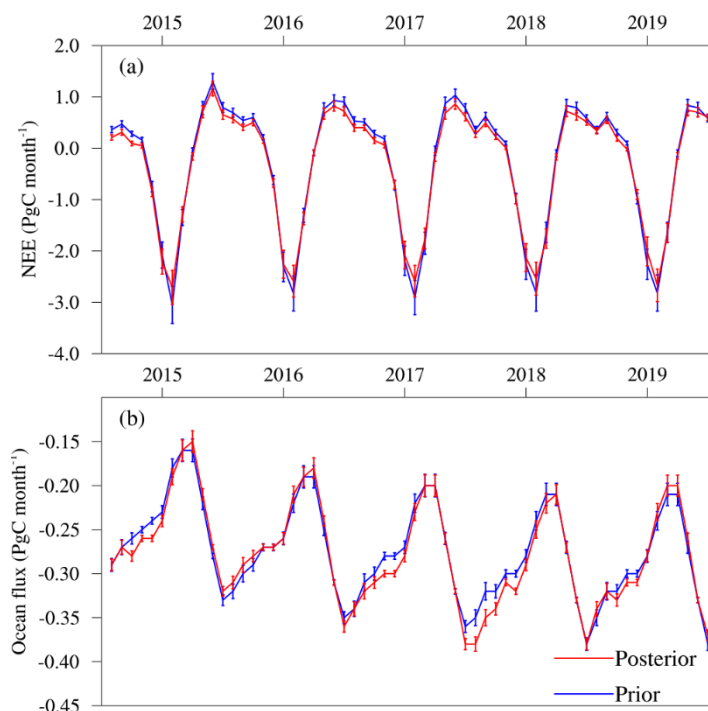
Figure 5. Monthly variations and corresponding uncertainties of global (a) NEE and (b) ocean carbon fluxes from prior and posterior estimates during 2015–2019.

4.1.3 Uncertainty evaluation

345 Figure 6 shows the global 5-year mean monthly prior and posterior uncertainties for NEE and ocean fluxes. Monthly means were calculated because uncertainties exhibit clear monthly characteristics. Figure A1 includes the daily uncertainties from prior and posterior estimates. The uncertainties were calculated from the ensemble of perturbations and prior fluxes using Eqs. (4), (10), and (11). As the prior ensemble dispersion was maintained when updated over time, the variation in uncertainties mainly depended on the prior fluxes and flux correlations between different grids. The pattern of NEE monthly uncertainties

350 was consistent with NEE monthly variation (Fig. 5a), with the largest sinks (June, July, and August) contributing to the largest uncertainties in the same months. For the ocean fluxes, uncertainties were much smaller than NEE. Because the flux initial ensemble of perturbations was generated through historical sampling, small uncertainties indicated relatively stable ocean fluxes over time. Large ocean uncertainties were concentrated in winter and summer. Large uncertainties in winter were related to the large ocean sink during that season, whereas large uncertainties in summer were caused by the high spatial correlations

355 between gridded fluxes.

Figure 7 shows the daily UR rates for NEE and ocean fluxes from 2015 to 2019, which varied prominently over time. The estimated URs depended strongly on the number of observations and specification of the observation errors, as well as the a priori error covariance matrix (Deng et al., 2014; Jiang et al., 2021). The UR values reflect the decrease of posterior uncertainties constrained by OCO-2 XCO_2 retrievals. The NEE URs ranged from 0.00 % to 27.90 %. The 0.00 % URs were

360 caused because no OCO-2 retrievals were provided in the inversion windows from April 21, 2015 to May 6, 2015 and from August 10, 2017 to September 6, 2017. Ocean URs were comparable to those over land, ranging from 0.00 % to 25.13 %. Due to the monthly prior ocean fluxes and 14-day inversion window, dates within the same month and the same inversion window shared common URs. Table 4 presents the global annual and annual mean prior uncertainties as well as the UR rates of NEE and ocean sinks during 2015–2019. Temporal correlations in the error covariance matrix were neglected, resulting in

365 discrepancies among the annual uncertainties and URs (Deng et al., 2014). The annual differences in uncertainty and UR decreased greatly when integrated over a year. The annual prior uncertainty of NEE was ~0.55 PgC yr^{-1}, and URs ranged from 7.28 % in 2015 to 8.45% in 2018. The annual prior uncertainties associated with ocean sinks were much smaller than those of NEE, and the annual total uncertainties of different years were probably consistent with each other. URs for ocean sinks were generally higher than those of NEE, with larger interannual variability, ranging from 6.59 % in 2014 to 10.49 % in

370 2016.
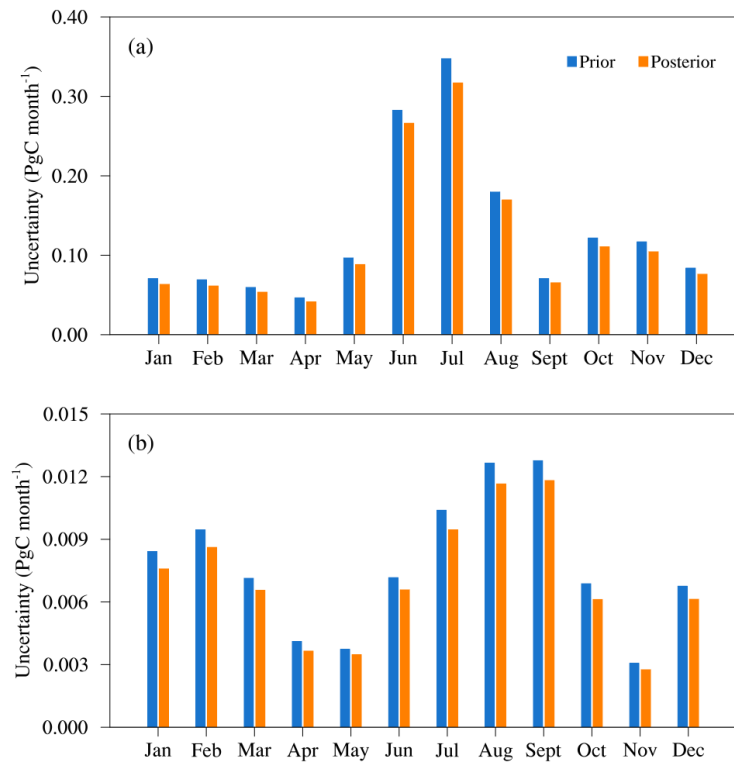
Figure 6. Global 5-year mean monthly prior and posterior uncertainties for (a) NEE and (b) ocean carbon fluxes.
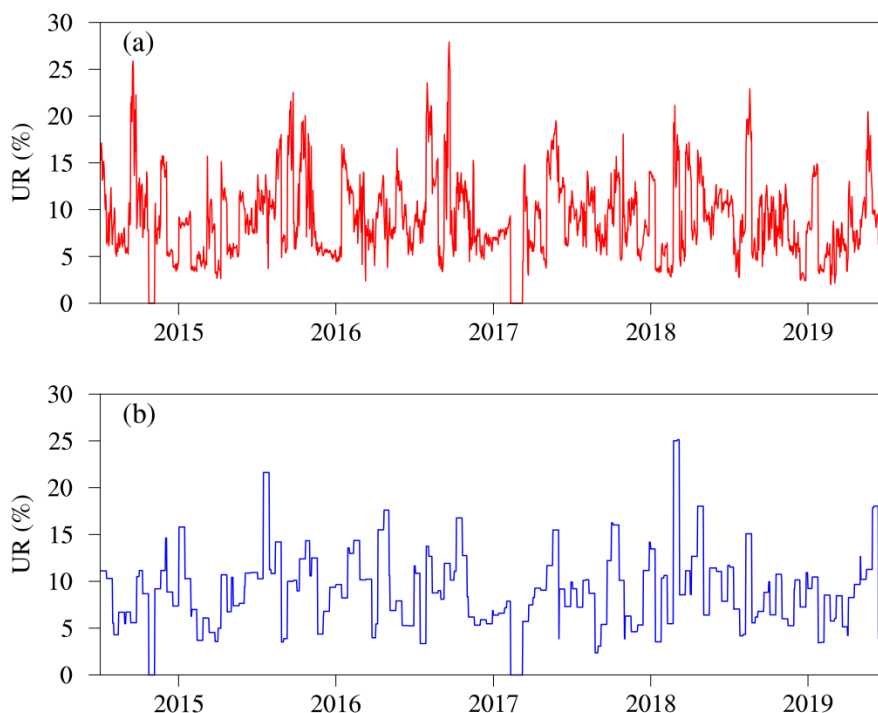
Figure 7. Daily uncertainty reduction (UR) rates for (a) NEE and (b) ocean carbon fluxes from 2015 to 2019.

375 **Table 4. Global annual and annual mean prior uncertainties and URs of NEE and ocean sinks during 2015–2019.**

	NEE		Ocean sink	
	Prior uncertainty (PgC yr^{-1})	UR (%)	Prior uncertainty (PgC yr^{-1})	UR (%)
2015	0.54	7.28	0.028	7.37
2016	0.53	8.14	0.028	10.49
2017	0.56	7.36	0.029	6.59
2018	0.56	8.45	0.029	10.07
2019	0.56	7.48	0.029	7.99
Annual mean	0.55	7.74	0.029	8.50

4.2 Regional fluxes

Figure 8 shows the global distributions of the prior and posterior annual mean NEE and ocean carbon fluxes during 2015–2019. For the prior NEE, carbon sinks mainly occurred over central and eastern North America, the central Amazon, southern South America, central Europe, most of Russia and China, central and southern Africa, and most of Australia. The area of the

380 terrestrial ecosystem carbon sources was much smaller than that of the sinks, which mainly occurred over western and southern

North America, northern South America, small areas in southern South America, northern and southern Europe, western Russia, scattered areas of northwestern and southwestern China, the Malay Archipelago, and the southern coast of Australia. After assimilating OCO-2 XCO$_2$ retrievals, sinks of central and northeastern North America were impaired whereas sinks of western, southeastern, and southern North America were strengthened. Meanwhile, sinks of the southern Amazon and eastern Brazil

385   were weakened. In Europe, the source was weaker and sink was stronger than prior ones. A widespread weakening of sink occurred in central Russia. Sinks of northeastern and eastern China as well as Australia were reinforced, sinks of Indochinese Peninsula were weakened nevertheless.

By contrast, the ocean carbon flux distribution was much simpler, with a clear characteristic that fluxes varied with latitude. The ocean flux sources mainly occurred in tropical oceans and high-latitude Southern Ocean, and the equatorial

390   Pacific was the most prominent source area for atmospheric CO$_2$. Sinks mainly occurred in mid-latitude regions of both hemispheres and high latitude Northern Ocean. After inversion, the overall pattern of ocean fluxes was preserved. The tropical sources were generally impaired, especially the eastern equatorial Pacific. Sinks of North Pacific were strengthened whereas sinks of southern Pacific were weakened. Besides, the northern and southern sinks of Atlantic as well as southern sinks of Indian Ocean were basically weaker than prior estimates. In general, the spatial distribution of NEE was far more complicated

395   than that of ocean carbon fluxes (Fig. 8), and the interannual variation of NEE was also stronger (Fig. A2). Therefore, the regional NEE requires more detailed analysis and attribution.

Table 5 lists the prior and posterior NEE for the 11 TransCom land regions. In each region, the prior NEE indicated a carbon sink. The powerful sinks occurred mainly in Asia, Africa, and North America, accounting for 45 %, 27 %, and 18 % of the total carbon sink. Among these regions, Boreal Asia had the strongest sink, followed by Temperate Asia, and the weakest

400   sink occurred in Tropical South America. After inversion, the posterior sinks of most regions were reinforced, except in Tropical South America and Boreal Asia. The European sink showed the largest increase of 0.29 PgC yr^{-1}. Clear sink enhancement also occurred in Temperate Asia and Northern Africa, of 0.17 and 0.10 PgC yr^{-1}, respectively. By contrast, Tropical South America shifted from a weak sink to a weak source. Harris et al. (2021) has pointed out that forests in the Brazilian Amazon were a net carbon source of 0.22 GtCO$_2$e yr^{-1} between 2001 and 2019, and estimated that commodity-driven

405   deforestation was the largest source of gross forest-related emissions. In Boreal Asia, the sink was weakened by 0.14 PgC yr^{-1}, but remained the strongest sink worldwide, followed by Temperate Asia and Northern Africa, accouning for 40 %, 27 %, and 17 % of the posterior global total sink. The interannual variability differed greatly for different regions. The Tropical South America had the most obvious interannual variability, followed by Temperate North America and Southern Africa (Fig. A3). The flux uncertainties in the Northern Hemisphere were generally higher than those in the Southern Hemisphere because of

410   the more complicated distribution of carbon sources and sinks in the Northern Hemisphere (Fig. 8). The four regions with the greatest uncertainties were Boreal Asia, Europe, Temperate North America, and Temperate Asia. Under the constraint of OCO-2 satellite observations, the posterior uncertainties of all 11 regions decreased. Australia, South Africa, and Tropical South America showed the clearest improvements where ground-based CO$_2$ observations are insufficient.
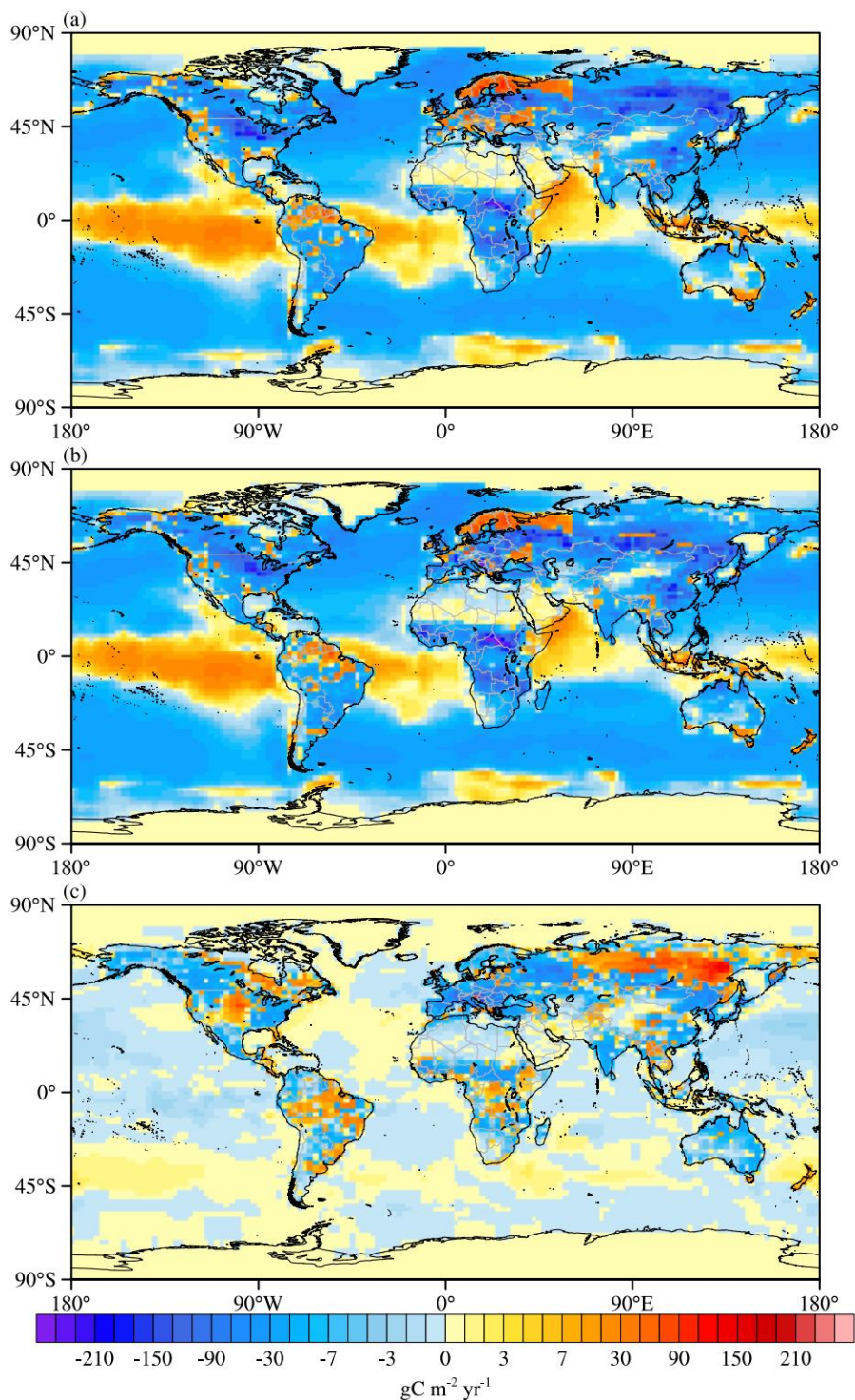
Figure 8. Global distributions of 5-year annual mean NEE and ocean carbon fluxes: (a) prior, (b) posterior, and (c) their differences (posterior – prior).

Table 5. Prior and posterior NEE values, and corresponding UR rates for the 11 TransCom land regions.

Region	NEE		UR (%)
	Prior (PgC yr^{-1})	Posterior (PgC yr^{-1})	
Boreal North America	−0.23 ± 0.078	−0.24 ± 0.072	7.7
Temperate North America	−0.37 ± 0.125	−0.42 ± 0.115	7.9
Tropical South America	−0.01 ± 0.046	0.01 ± 0.042	9.5
Temperate South America	−0.17 ± 0.049	−0.17 ± 0.045	8.9
Northern Africa	−0.53 ± 0.046	−0.63 ± 0.042	8.7
Southern Africa	−0.40 ± 0.025	−0.41 ± 0.023	9.7
Boreal Asia	−0.88 ± 0.201	−0.74 ± 0.185	7.9
Temperate Asia	−0.56 ± 0.082	−0.73 ± 0.075	8.5
Tropical Asia	−0.07 ± 0.020	−0.08 ± 0.018	9.0
Australia	−0.05 ± 0.011	−0.09 ± 0.010	9.9
Europe	−0.12 ± 0.138	−0.41 ± 0.127	8.0

4.3 Tibetan Plateau fluxes

The Tibetan Plateau was demonstrated to act as a carbon sink through remote sensing observations, ecosystem models, and
420   atmospheric inversions during the 1980s and 1990s (Piao et al., 2009). Recent flux observations and field soil carbon data have
also confirmed the carbon sink function of the Tibetan Plateau (Kato et al., 2006; Li et al., 2016; Ding et al., 2017). The carbon
estimates of the Tibetan Plateau reported in this study are consistent with those reported in previous studies. The prior annual
mean NEE was –52.65 TgC yr^{-1}, whereas the posterior NEE was weakened to –49.52 TgC yr^{-1} during 2015–2019. Figure 9
shows the 5-year annual and seasonal variations of NEE on the Tibetan Plateau. The prior NEE ranged from –38.35 TgC yr^{-1}
425   in 2015 to –67.47 TgC yr^{-1} in 2017, whereas the posterior NEE ranged from –30.39 TgC yr^{-1} in 2015 to –68.87 TgC yr^{-1} in
2017. The posterior NEE were impaired every year except in 2017, with the largest change occurring in 2015. The prior
uncertainties of annual NEE on the Tibetan Plateau were 14.83, 13.54, 15.92, 15.77, and 15.77 TgC yr^{-1}, respectively, during
2015–2019. After inversion, these uncertainties were reduced by 8.54 %, 9.06 %, 8.20 %, 8.70 %, and 6.94 %, respectively.
The UR rates on the Tibetan Plateau were comparable to that observed globally and regionally.
430   The NEE on the Tibetan Plateau showed a clear seasonal cycle. The ecosystem acted as a carbon sink from May to
September and as a carbon source from January to April and October to December, with the peak monthly uptake occurring
in July. The prior annual mean sink from May to September and source from January to April and October to December were
estimated to be –101.65 and 49.00 TgC yr^{-1}, which contributed to forming a net annual sink. The corresponding posterior
values were –104.40 and 54.88 TgC yr^{-1}, respectively. Both the posterior seasonal sink and source were amplified, whereas
435   the increased amplitude of the source was stronger than that of the sink, resulting in a decrease in the posterior annul net sink.
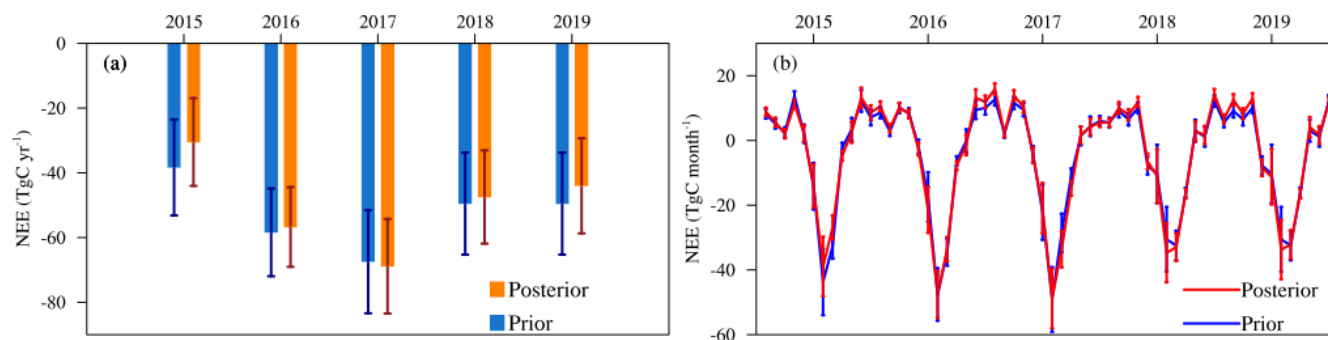
Figure 9. Prior and posterior NEE on the Tibetan Plateau during 2015–2019. (a) Annual variation. (b) Seasonal cycle.

Figure 10 shows the 5-year mean spatial distribution of NEE on the Tibetan Plateau during 2015–2019. Previous studies have reported clear regional heterogeneity in the spatial distribution of carbon sinks on the Tibetan Plateau, with significantly

440   stronger carbon sinks in eastern alpine meadows than in western alpine steppes (Jin et al., 2015; Ding et al., 2017). Our estimates were consistent with these findings. Overall, the Tibetan Plateau ecosystem tended to take up carbon; the eastern plateau was the strongest carbon sink, whereas small parts of the southeastern and northern regions emitted CO_2. The eastern distribution was dramatically modified after inversion, with impaired central sinks and amplified surrounding sinks. The central and northern sinks of the plateau were weakened, and the western and southern sinks were slightly strengthened. This

445   spatial heterogeneity in the distribution of carbon sources and sinks on the Tibetan Plateau is related to water conditions. Alpine meadows face lower drought stress than alpine steppes; therefore, the increased vegetation productivity of alpine meadows due to warming is greater than that of alpine steppes, in turn leading to more organic carbon fixation by vegetation input into the soil (Ding et al., 2017; Du et al., 2018; Hopping et al., 2018). The results of field control experiments on the Tibetan Plateau have also shown that warming promotes the net exchange of carbon fluxes in meadow ecosystems with better

450   water conditions, whereas it inhibits carbon fixation in arid steppes (Ganjurjav et al., 2018).
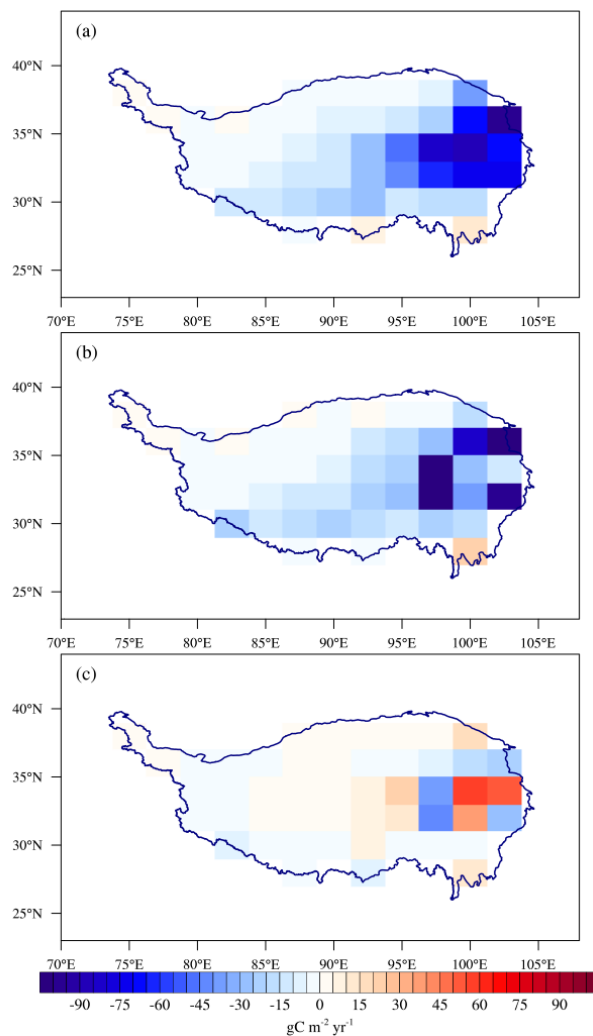
Figure 10. Five-year mean spatial distributions of NEE on the Tibetan Plateau during 2015–2019 based on (a) prior NEE, (b) posterior NEE, and (c) their difference (posterior – prior).

5 Dataset evaluation

5.1 Evaluation using independent OCO-2 observations

We evaluated model simulated XCO_2 against independent OCO-2 retrievals to indirectly verify the posterior NEE and ocean carbon fluxes. Figure 11 compares prior and posterior simulated XCO_2 with independent OCO-2 XCO_2 observations. The simulated and observed XCO_2 values were daily averages; daily statistics were calculated using all observations within a single day. The prior simulated XCO_2 were generally higher than OCO-2 observations, and the deviation accumulated with forward model integration. Since 2016, RMSE, BIAS, and MAE remained above 1.5, 1.0, and 1.5 ppm, respectively. By 2018, these statistics reached 2.3, 2.0, and 2.0 ppm, respectively. Table 6 shows the 5-year annual mean statistics. After inversion,

simulated CO_2 concentrations decreased, especially at the surface (Fig. A4); posterior RMSE, BIAS, and MAE were greatly improved, with RMSE decreasing from 2.12 to 1.27 ppm, BIAS from 1.62 to 0.33 ppm, and MAE from 1.80 to 0.95 ppm. There were no significant changes in CORR before or after inversion. These results show that satellite observations were well

465   absorbed by the inversion system, such that the NEE and ocean carbon fluxes were corrected effectively.
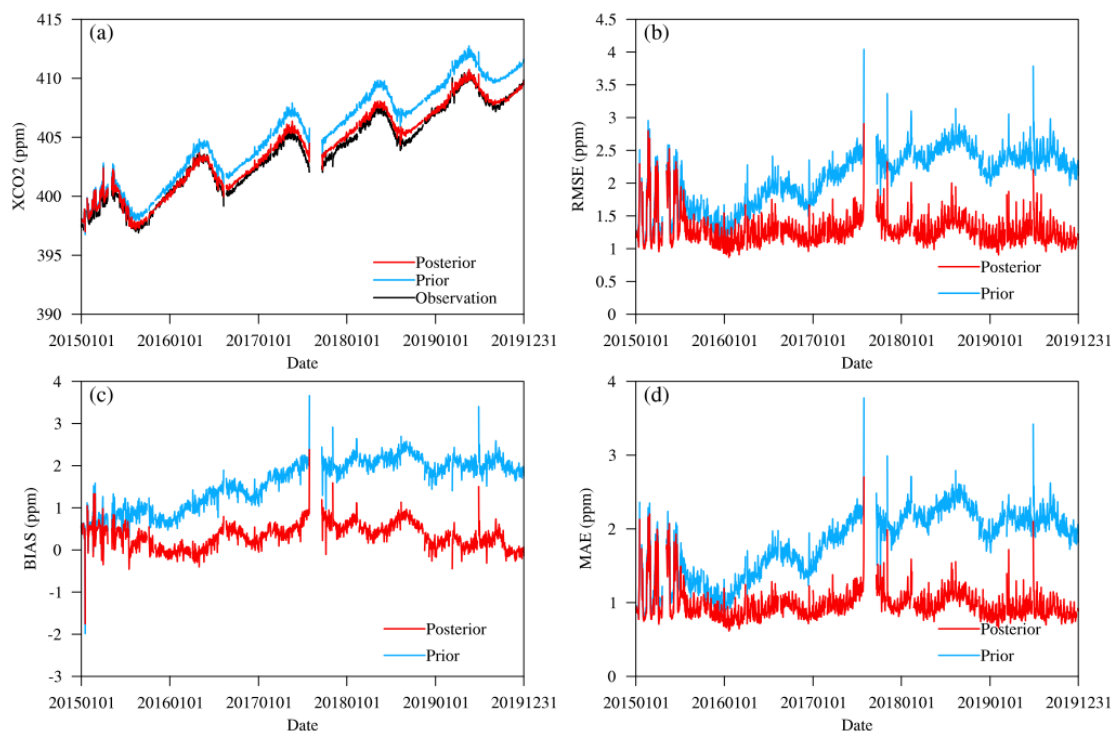
Figure 11. Comparison of prior and posterior simulated XCO₂ with independent OCO-2 XCO₂ observations. (a) Time series of simulated and observed XCO₂, (b) RMSE, (c) BIAS, and (d) MAE of simulated and observed XCO₂.

Table 6. Statistics for simulated XCO₂ and OCO-2 independent XCO₂ observations.

RMSE (ppm)		BIAS (ppm)		MAE (ppm)		CORR	
Prior	Posterior	Prior	Posterior	Prior	Posterior	Prior	Posterior
2.12	1.27	1.62	0.33	1.80	0.95	0.95	0.95

470   **5.2 Evaluation using TCCON observations**

Table 7 lists the statistics for simulated XCO₂ and TCCON observed XCO₂. The prior model-simulated XCO₂ were generally higher than TCCON observations except at the HeiFei site, and BIAS exceeded 2 ppm at many sites (e.g., Ny Ålesund, Garmisch, and Nicosia sites). RMSE, BIAS, and MAE between prior simulated and observed XCO₂ were 1.89, 1.51, and 1.63 ppm worldwide. This result agrees with the flux analysis presented in Sec. 4.1, which indicated that the global carbon sink was

475   underestimated. The error of model simulations was generally larger in the Northern Hemisphere than in the Southern

Hemisphere, due to the more complex carbon flux pattern in the Northern Hemisphere (Wang et al., 2019). After inversion, the global carbon sink was reinforced, contributing to a more reasonable atmospheric CO_2 simulation. The posterior RMSE, BIAS, and MAE were 1.06, 0.12, and 0.81 ppm, decreasing by 44 %, 92 %, and 50 %, respectively, compared to the prior statistics, demonstrating the optimization of posterior fluxes through absorbing OCO-2 satellite observations.

480   Figure 12 shows the time series of prior and posterior simulated XCO_2 and observed XCO_2 at 30 TCCON sites. The global CO_2 concentrations generally increased over time. In the Northern Hemisphere, CO_2 concentrations showed a strong seasonal cycle. The strong source in winter caused high CO_2 concentrations, whereas the strong sink in summer caused low CO_2 concentrations. In the Southern Hemisphere, the seasonal cycle was much weaker than in the Northern Hemisphere, and became less clear as latitude increased. The Southern Hemisphere is mainly covered by ocean, and the seasonal variation in

485 ocean fluxes was much less pronounced than NEE (Fig. 5), with a less complex spatial distribution than that over land (Fig. 8), contributing in turn to the weak seasonal cycle of CO_2 concentrations in the Southern Hemisphere. Generally, posterior simulated XCO_2 characterized the temporal variation characteristics of CO_2 observations.

     At most sites, prior simulated XCO_2 were larger than TCCON observations. The overestimation of winter CO_2 concentrations in the Northern Hemisphere was very clear, especially in the mid- and high latitudes. After inversion, the

490 simulated concentrations agreed better with TCCON observations (Fig. 13). The overestimation of winter CO_2 concentrations at mid- and high latitudes of the Northern Hemisphere was also well mitigated due to the weakening of winter carbon sources (Sec. 4.1.2). The inversion results were not ideal at the Jet Propulsion Laboratory, Caltech, and HeFei sites. At these three sites, prior simulated XCO_2 were close to the TCCON observations, whereas posterior simulations were about 1 ppm smaller than the TCCON observations, suggesting that carbon sinks were overestimated or carbon sources were underestimated. This may

495 be related to biases of OCO-2 retrievals (O'dell et al., 2018). Besides, the resolution of the Tan-Tracker inversion system is 2° latitude × 2.5° longitude; therefore, it cannot achieve ideal results at every site worldwide. Improvements of inversion resolution and observation quality are necessary to infer fluxes at finer regional scales.

Table 7. Geographic locations of TCCON sites used for validation, and statistics used to compare simulated XCO₂ and TCCON XCO₂ observations. Sites are listed according to latitude from north to south.

Station	Lat.	Long.	RMSE (ppm)		BIAS (ppm)		MAE (ppm)	
			Prior	Posterior	Prior	Posterior	Prior	Posterior
Eureka	80.05	−86.42	1.57	1.13	1.02	−0.61	1.30	0.86
Ny Ålesund	78.90	11.92	2.62	1.27	2.47	0.96	2.47	1.08
Sodankylä	67.37	26.63	2.46	1.15	2.28	0.81	2.31	0.94
East Trout Lake	54.35	−104.99	2.46	1.05	2.25	0.42	2.28	0.81
Bialystok	53.23	23.02	1.90	0.93	1.68	0.51	1.70	0.73
Bremen	53.10	8.85	2.19	1.09	1.96	0.55	1.98	0.87
Karlsruhe	49.10	8.44	2.21	1.07	1.92	0.48	1.96	0.87

Paris	48.97	2.36	1.96	1.46	1.06	–0.32	1.58	1.14
Orléans	47.97	2.11	2.45	1.17	2.26	0.86	2.26	0.95
Garmisch	47.48	11.06	2.56	1.19	2.34	0.84	2.35	1.00
Zugspitze	47.42	10.98	1.49	0.80	1.20	–0.21	1.25	0.62
Park Falls	45.95	–90.27	1.85	0.81	1.48	0.10	1.57	0.59
Rikubetsu	43.46	143.77	2.20	1.09	1.83	0.32	1.87	0.75
Lamont	36.60	–97.49	1.60	0.70	1.37	–0.02	1.42	0.55
Anmeyondo	36.50	126.33	1.35	1.00	0.91	–0.10	1.11	0.77
Tsukuba	36.05	140.12	2.06	1.24	1.64	0.14	1.77	0.92
Nicosia	35.14	33.38	2.52	0.74	2.46	0.11	2.46	0.61
Edwards	34.96	–117.88	1.93	0.75	1.81	0.34	1.81	0.59
Jet Propulsion Laboratory	34.20	–118.18	0.98	1.40	0.49	–1.10	0.80	1.16
Caltech	34.14	–118.13	1.13	1.66	0.17	–1.24	0.90	1.37
Saga	33.24	130.29	1.62	1.10	1.09	–0.51	1.30	0.89
Hefei	31.91	117.17	1.21	1.74	–0.08	–1.24	0.93	1.47
Izana	28.30	–16.48	1.72	0.85	1.46	–0.32	1.50	0.72
Burgos	18.53	120.65	2.01	0.92	1.83	0.00	1.84	0.71
Manaus	–3.21	–60.60	1.12	0.97	0.64	0.36	0.89	0.79
Ascension Island	–7.92	–14.33	2.05	1.20	1.83	0.89	1.83	0.98
Darwin	–12.46	130.89	1.56	0.99	1.39	0.17	1.43	0.76
Réunion Island	–20.90	55.49	1.53	1.01	1.27	0.18	1.32	0.77
Wollongong	–34.41	150.88	1.34	0.86	1.09	–0.12	1.20	0.66
Lauder	–45.04	169.68	1.73	0.57	1.55	0.34	1.56	0.47
Global mean	–	–	1.89	1.06	1.51	0.12	1.63	0.81
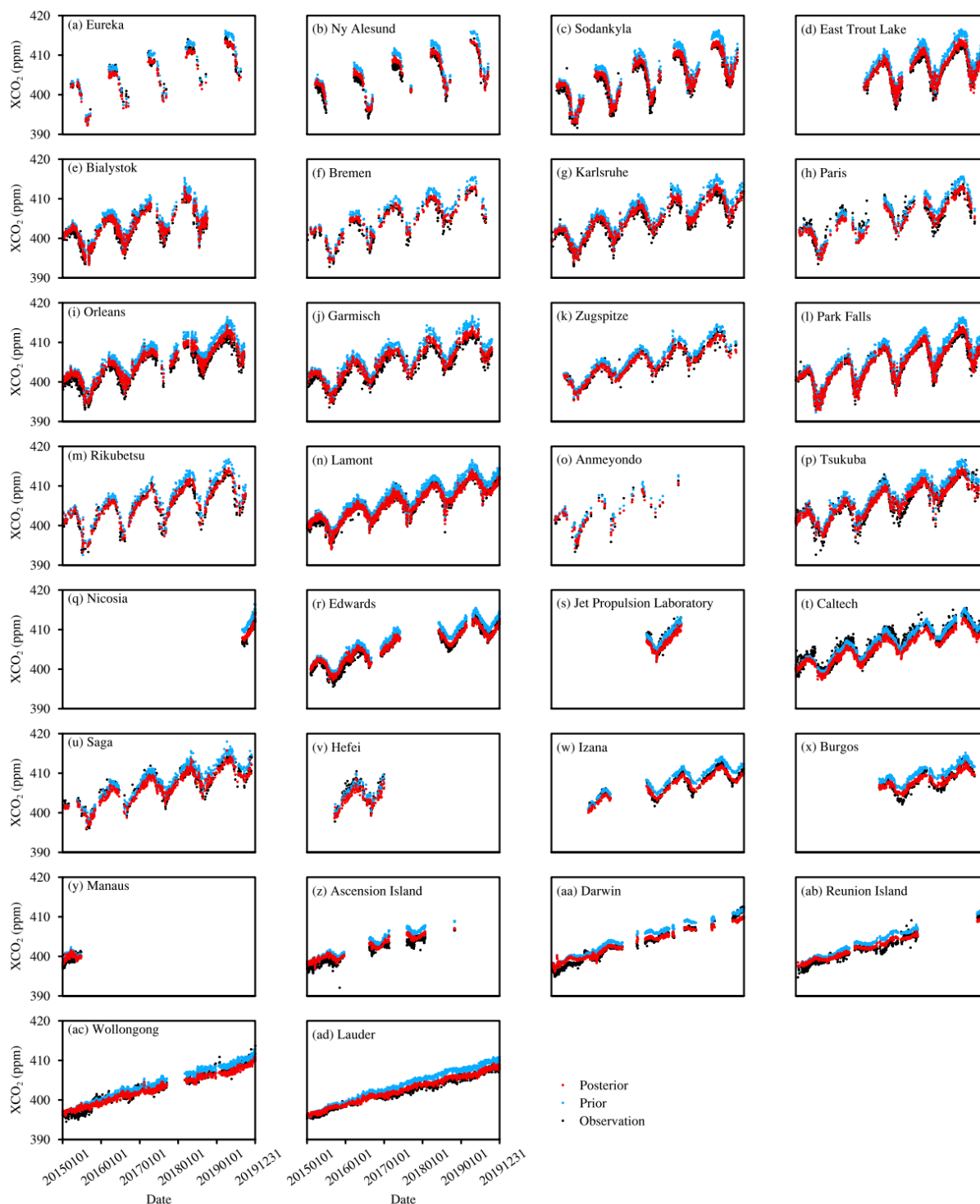
500

Figure 12. Time series of prior and posterior simulated XCO₂ and XCO₂ observations at 30 TCCON sites. Sites are sorted according to latitude from north to south.
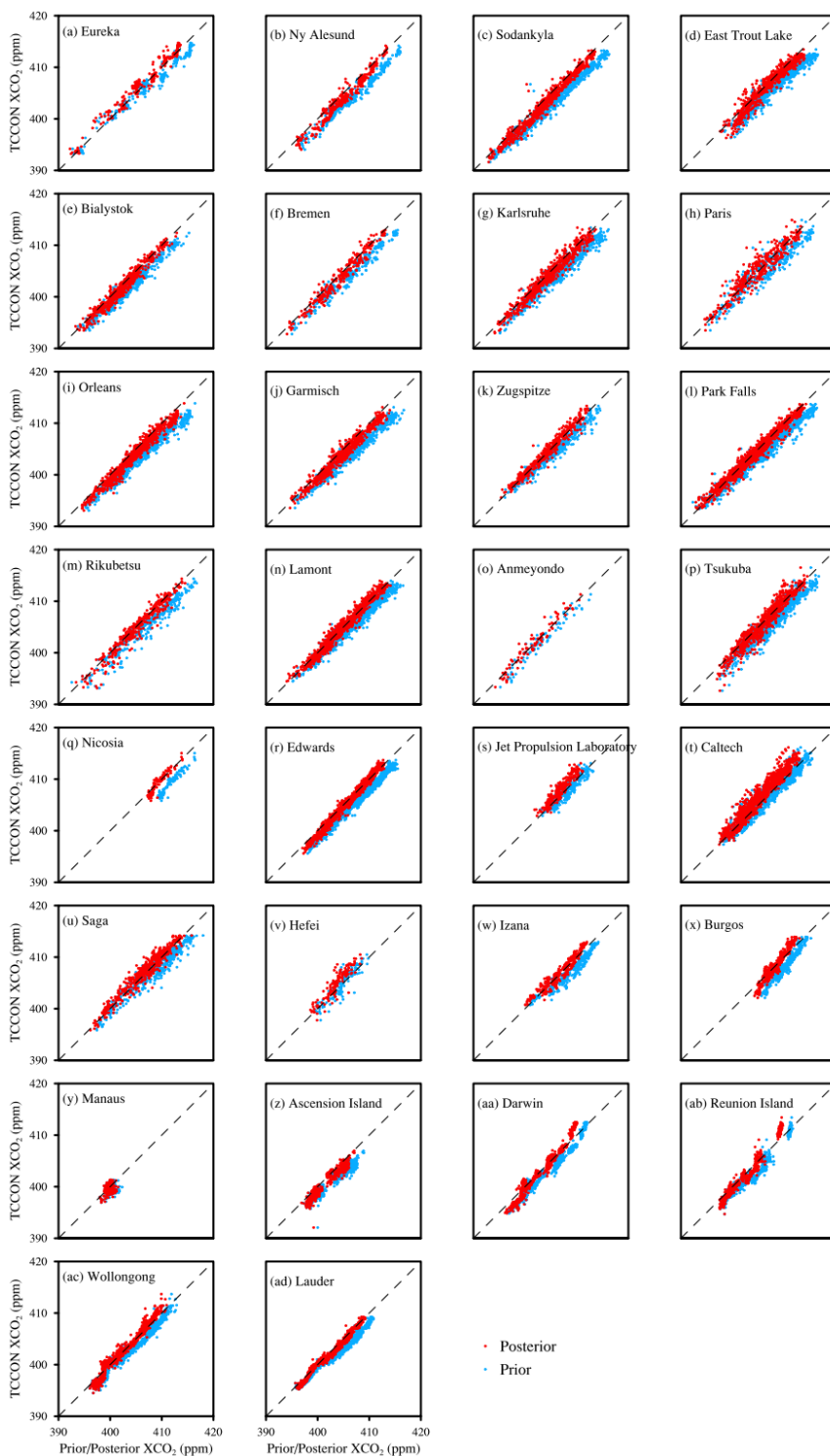
Figure 13. Scatter plots of prior and posterior simulated XCO₂ and XCO₂ observations at 30 TCCON sites. Sites are sorted according to latitude from north to south.

6 Discussion

The atmospheric CO_2 observations assimilated in this study were OCO-2 XCO_2 retrievals. Although satellite observations have better spatial coverage than ground-based observations, they remain unable to continuously monitor CO_2 concentrations with global coverage, resulting in observational gaps. Spatial and temporal gaps in ground- and space-based observations can
510   introduce artifacts into flux estimates, leading to difficulties in constraining carbon fluxes at regional scales (Basu et al., 2018; Byrne et al., 2017; Liu et al., 2014). Advances in satellite retrieval algorithms allow significant improvements in the consistency of space- and surface-based flux constraints (Byrne et al., 2020). The simultaneous assimilation of ground- and space-based atmospheric CO_2 observations will be carried out in the Tan-Tracker inversion system, expecting more precise estimation of regional fluxes.

515   In this study, we optimized terrestrial ecosystem carbon fluxes and ocean carbon fluxes, while assuming no error in other emission inventories. As the largest emission sector, global fossil CO_2 emissions are estimated with an uncertainty at ± 5 % according to GCB2020 (Friedlingstein et al., 2020). However, uncertainties of national bottom-up fossil fuel emissions vary across countries according to data collection and management practices (Andres et al., 2014; Marland, 2008; Oda et al., 2018a). Inaccuracies in fossil CO_2 emissions are added to NEE optimization based on our assumption, which may cause bias in NEE
520   estimates. Fossil CO_2 emissions are anthropogenic, whereas NEE are natural emissions or uptakes; both have different emission characteristics and spatial distributions. In a future study, we plan to simultaneously optimize fossil emissions and NEE to distinguish errors from anthropogenic and natural sectors.

The treatment of various errors during inversion also requires improvement. The transport model is assumed to have no error, and all errors associated with simulated CO_2 are attributed to the initial CO_2 concentrations and carbon fluxes. An
525   independent and comprehensive quantification of the systematic errors of transport models is required to distinguish CO_2 simulation errors from different sources. To account for prior flux uncertainties, we used 36 samples to approximate the prior error covariance matrix and updated the matrix over time. To date, there is no consensus on the accurate calculation of prior uncertainties. In this study, when gridded flux uncertainties were integrated over space and time, only the spatial correlation of gridded fluxes was considered, whereas the temporal correlation was omitted. However, the gridded fluxes were correlated
530   in time according to their diffusive and accumulative characteristics, resulting in underestimated monthly or yearly uncertainties. Further efforts are required to improve confidence in the resulting posterior fluxes and corresponding uncertainties.

The global-scale flux inversion performed in this study had a spatial resolution of 2° latitude × 2.5° longitude. Inversions with this resolution are feasible and effective for large and global regions. However, the requirements for fine and accurate
535   regional inversions are increasing, and the present resolution cannot meet the stricter standards anticipated in the future. Therefore, we plan to perform finer inversions at regional scales to obtain a better understanding of regional carbon cycles.

7 Data availability

The dataset is available in the National Tibetan Plateau/Third Pole Environment Data Center and can be accessed at https://doi.org/10.11888/Meteoro.tpdc.271317 (Jin et al., 2021). As the satellite XCO_2 retrievals, carbon fluxes, and meteorological

540 data are persistently improving and updating, we plan to update the dataset annually in the future, aiming to support current scientific research and policy making.

8 Conclusion

Here we present a global and regional resolved NEE and ocean carbon flux dataset during 2015–2019. The dataset was generated by the Tan-Tracker inversion system constrained by OCO-2 XCO_2 retrievals. We qualitatively validated the

545 posterior fluxes by comparing the posterior simulated CO_2 concentrations with OCO-2 independent retrievals and TCCON observations. After inversion, posterior RMSE, BIAS, and MAE for simulated and OCO-2 XCO_2 were greatly improved, with RMSE decreasing from 2.12 to 1.27 ppm, BIAS from 1.62 to 0.33 ppm, and MAE from 1.80 to 0.95 ppm. The posterior RMSE, BIAS, and MAE for simulated and TCCON XCO_2 were 1.06, 0.12, and 0.81 ppm, decreasing by 44 %, 92 %, and 50 %, respectively, compared to the prior statistics. Both validations demonstrated the optimization of posterior fluxes through

550 absorbing OCO-2 satellite observations. We described the characteristics of the dataset at the global, regional and Tibetan Plateau scales from aspects of carbon budget, annual and seasonal variations, and spatial distribution. Also, the posterior fluxes were assessed through comparisons with other flux estimates, such as GCB2020, CT2019B, and JCS data. The posterior 5-year annual mean global AGR was 5.35 PgC yr^{-1} and within the uncertainty of the GCB2020 estimate. The posterior annual mean NEE and ocean carbon fluxes were –4.07 and –3.33 PgC yr^{-1}, respectively. Regional fluxes are analysed based on

555 TransCom partition. All 11 land regions acted as carbon sinks apart from Tropical South America, which was almost neutral. The strongest carbon sinks were seen in Boreal Asia, followed by Temperate Asia and North Africa. The Tibetan Plateau ecosystem was estimated as a carbon sink as a whole, absorbing –49.52 TgC yr^{-1} for the annual mean. The sinks in the eastern alpine meadows were much stronger than that in the western steppes, while sporadic areas in the southeastern and northern regions acted as sources. This dataset can help understand global and regional carbon distribution and its variability, support

560 the formulation of climate policies, and make well-informed projections under future climate change.

Appendix A

In the Appendix, we include the table and figures to support the main text.

Table A1. Global annual carbon flux estimates from various sectors and AGR during 2015–2019. The NEE and ocean carbon fluxes here refer to posterior values.

CO_2 emissions and uptakes (PgC yr^{-1})	2015	2016	2017	2018	2019

NEE	–4.05	–3.17	–4.15	–4.73	–4.28
Ocean carbon fluxes	–2.90	–3.17	–3.47	–3.64	–3.47
Fossil fuel emissions	9.31	9.35	9.45	9.67	9.72
Biomass burning emissions	2.10	1.74	1.79	1.70	2.14
Biofuel burning emissions	0.82	0.82	0.82	0.82	0.82
Ship emissions	0.27	0.27	0.27	0.27	0.27
Aircraft emissions	0.28	0.29	0.31	0.32	0.32
Chemical source	1.11	1.11	1.11	1.11	1.11
Surface correction	–1.14	–1.14	–1.14	–1.15	–1.15
AGR	5.81	6.11	4.98	4.38	5.49

565
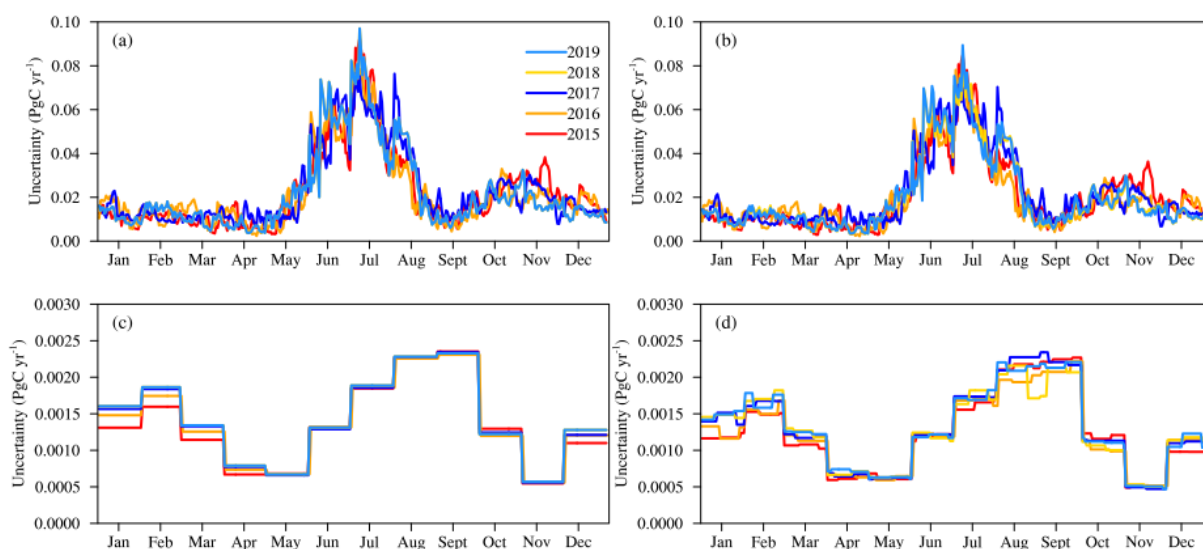
Figure A1. Daily uncertainties for (a) prior NEE, (b) posterior NEE, (c) prior ocean carbon fluxes, and (d) posterior ocean carbon fluxes from 2015 to 2019.
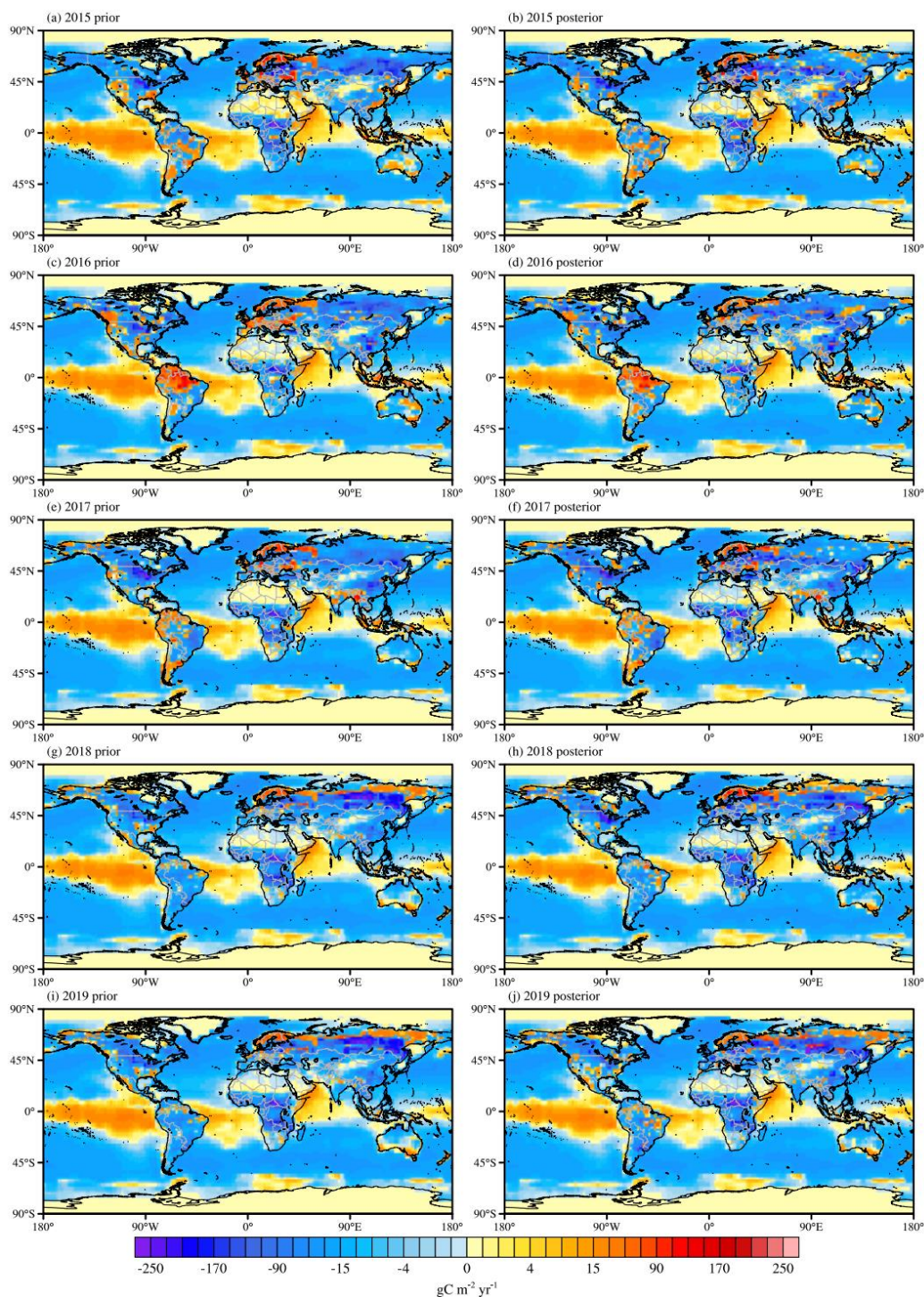
Figure A2. Spatial distributions of prior and posterior NEE plus ocean carbon fluxes from 2015 to 2019. The first column plots (a, c, e, g, i) denote the prior distributions and the second column plots (b, d, f, h, j) denote the posterior distributions.
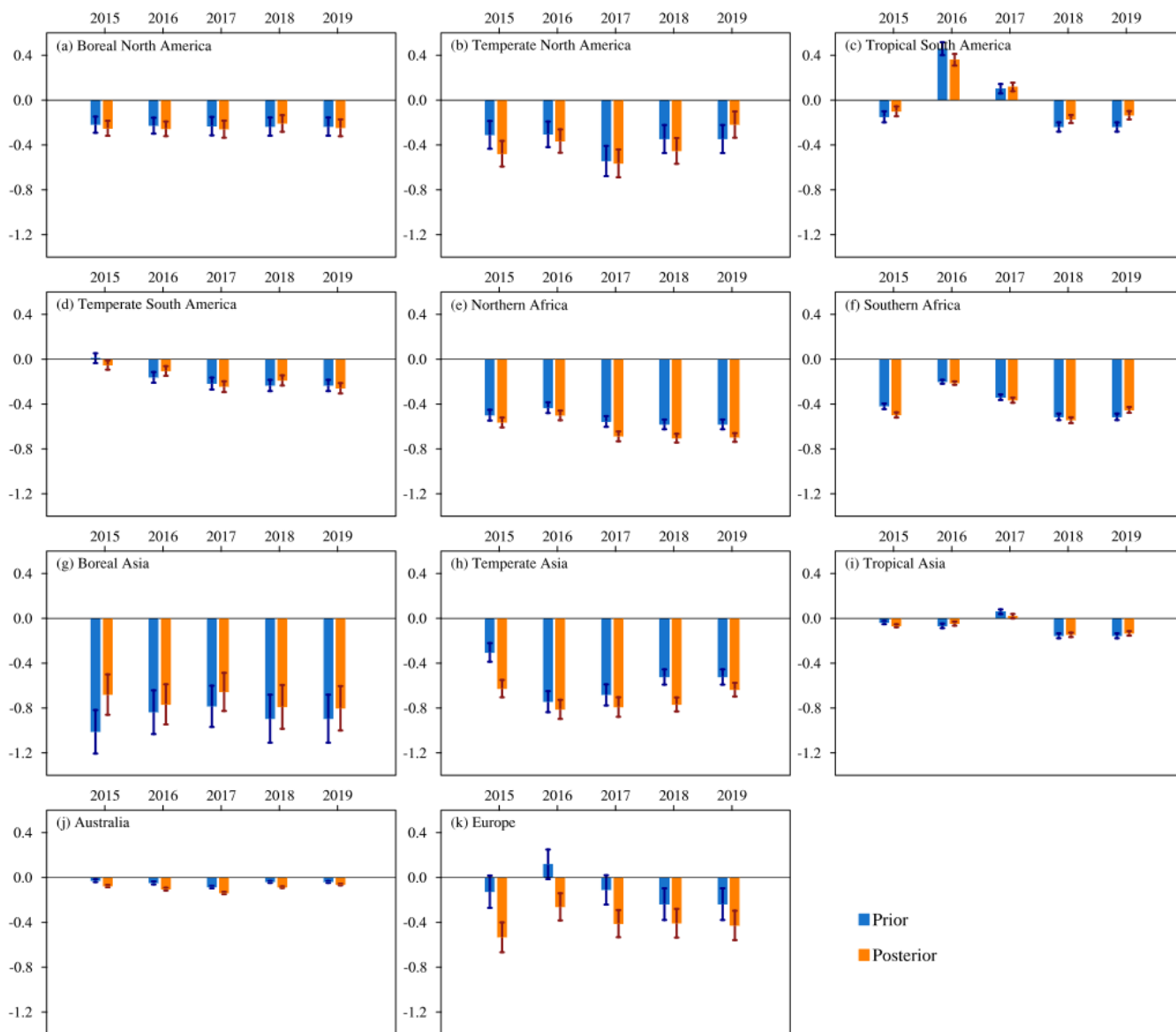
Figure A3. Prior and posterior interannual variations of NEE in the 11 TransCom land regions from 2015 to 2019.
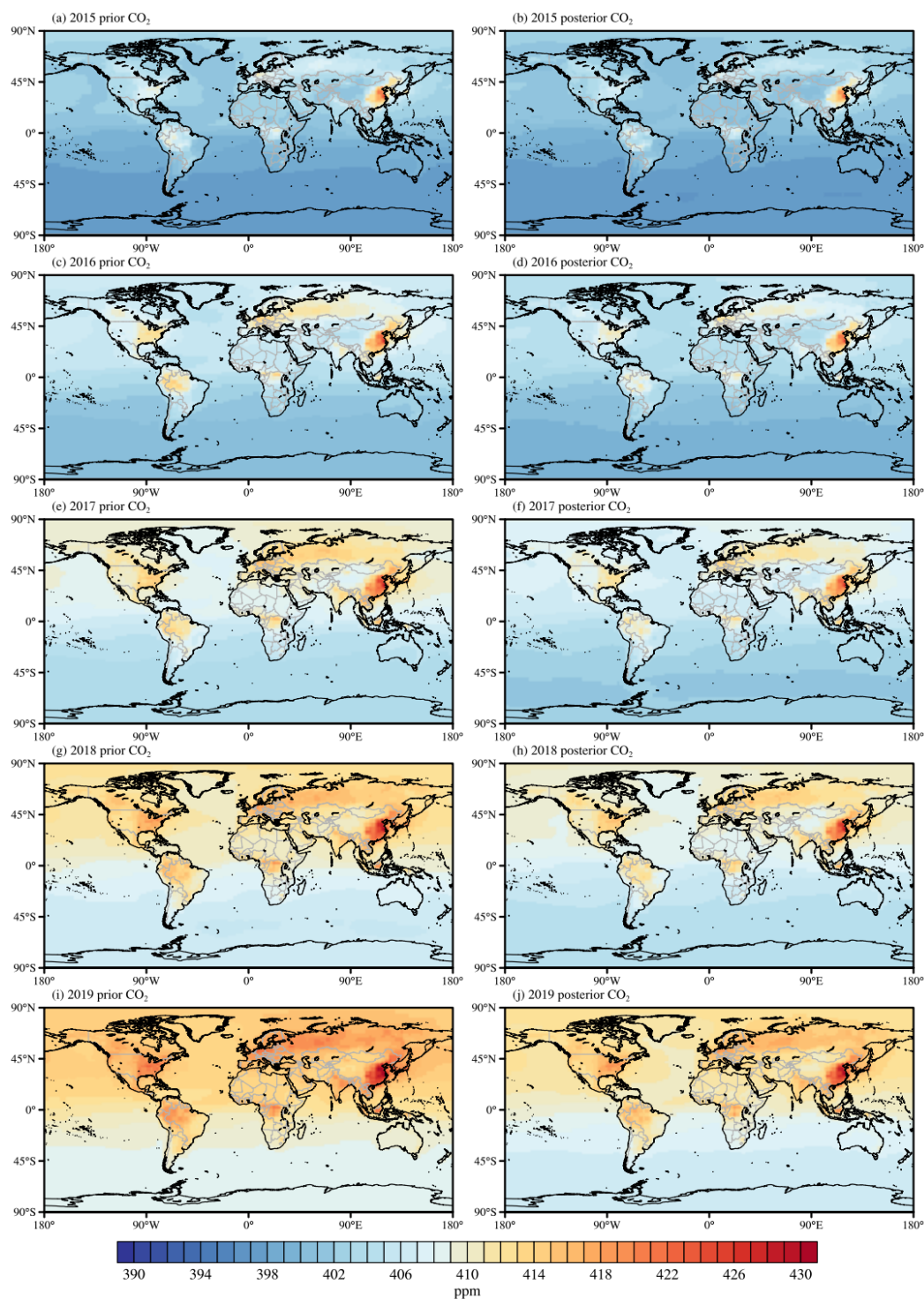
Figure A4. Spatial distributions of prior and posterior simulated surface CO₂ concentrations from 2015 to 2019. The first column plots (a, c, e, g, i) denote the prior distributions and the second column plots (b, d, f, h, j) denote the posterior distributions.

575

Author contributions. TX conceptualized, administrated, and supervised the research, and acquired funds for it. JZ, HR, and FY made investigations, constructed the inversion system, and visualized the data. JZ created the dataset. JZ and FY made formal analysis of it. TX and LX developed the methodology. TX, LX, and MH provided necessary resources. JZ and CC validated the data. JZ wrote the original manuscript draft. TX, LX, and FY reviewed and edited the original manuscript draft.

Competing interest. The authors declare that they have no conflict of interest.

Acknowledgements. The authors acknowledge all of the atmospheric data providers of TCCON GGG 2014 version. CarbonTracker CT2019B results are provided by NOAA ESRL, Boulder, Colorado, USA from the website at http://carbontracker.noaa.gov. The OCO-2 data are provided by the ACOS/OCO-2 project at the Jet Propulsion Laboratory, California Institute of Technology, and can be obtained from the data archive at the NASA Goddard Earth Science Data and Information Services Center.

Financial support. This work was supported by the National Key Research and Development Program of China [2016YFA0600203], the National Natural Science Foundation of China [41575100], and the Key Research Program of Frontier Sciences, Chinese Academy of Sciences (CAS) [QYZDYSSW-DQC012].

References

Andres, R. J., Boden, T. A., and Higdon, D.: A new evaluation of the uncertainty associated with CDIAC estimates of fossil fuel carbon dioxide emission, Tellus Series B-Chemical and Physical Meteorology, 66, 10.3402/tellusb.v66.23616, 2014.

Basu, S., Baker, D. F., Chevallier, F., Patra, P. K., Liu, J., and Miller, J. B.: The impact of transport model differences on CO2 surface flux estimates from OCO-2 retrievals of column average CO2, Atmospheric Chemistry and Physics, 18, 7189-7215, 10.5194/acp-18-7189-2018, 2018.

Basu, S., Guerlet, S., Butz, A., Houweling, S., Hasekamp, O., Aben, I., Krummel, P., Steele, P., Langenfelds, R., Torn, M., Biraud, S., Stephens, B., Andrews, A., and Worthy, D.: Global CO2 fluxes estimated from GOSAT retrievals of total column CO2, Atmospheric Chemistry and Physics, 13, 8695-8717, 10.5194/acp-13-8695-2013, 2013.

Byrne, B., Jones, D. B. A., Strong, K., Zeng, Z. C., Deng, F., and Liu, J.: Sensitivity of CO2 surface flux constraints to observational coverage, Journal of Geophysical Research-Atmospheres, 122, 6672-6694, 10.1002/2016jd026164, 2017.

Byrne, B., Liu, J., Lee, M., Baker, I., Bowman, K. W., Deutscher, N. M., Feist, D. G., Griffith, D. W. T., Iraci, L. T., Kiel, M., Kimball, J. S., Miller, C. E., Morino, I., Parazoo, N. C., Petri, C., Roehl, C. M., Sha, M. K., Strong, K., Velazco, V. A., Wennberg, P. O., and Wunch, D.: Improved Constraints on Northern Extratropical CO2 Fluxes Obtained by Combining Surface-Based and Space-Based Atmospheric CO2 Measurements, Journal of Geophysical Research-Atmospheres, 125, 10.1029/2019jd032029, 2020.

Chen, H., Zhu, Q., Peng, C., Wu, N., Wang, Y., Fang, X., Gao, Y., Zhu, D., Yang, G., Tian, J., Kang, X., Piao, S., Ouyang, H., Xiang, W., Luo, Z., Jiang, H., Song, X., Zhang, Y., Yu, G., Zhao, X., Gong, P., Yao, T., and Wu, J.: The impacts of climate change and human activities on biogeochemical cycles on the Qinghai-Tibetan Plateau, Global Change Biology, 19, 2940-2955, 10.1111/gcb.12277, 2013.

Chevallier, F., Palmer, P. I., Feng, L., Boesch, H., O'Dell, C. W., and Bousquet, P.: Toward robust and consistent regional CO2 flux estimates from in situ and spaceborne measurements of atmospheric CO2, Geophysical Research Letters, 41, 1065-1070, 10.1002/2013gl058772, 2014.

Chevallier, F., Remaud, M., O'Dell, C. W., Baker, D., Peylin, P., and Cozic, A.: Objective evaluation of surface- and satellite-driven carbon dioxide atmospheric inversions, Atmospheric Chemistry and Physics, 19, 14233-14251, 10.5194/acp-19-14233-2019, 2019.

Chevallier, F., Ciais, P., Conway, T. J., Aalto, T., Anderson, B. E., Bousquet, P., Brunke, E. G., Ciattaglia, L., Esaki, Y., Froehlich, M., Gomez, A., Gomez-Pelaez, A. J., Haszpra, L., Krummel, P. B., Langenfelds, R. L., Leuenberger, M., Machida, T., Maignan, F., Matsueda, H., Morgui, J. A., Mukai, H., Nakazawa, T., Peylin, P., Ramonet, M., Rivier, L., Sawa, Y., Schmidt, M., Steele, L. P., Vay, S. A., Vermeulen, A. T., Wofsy, S., and Worthy, D.: CO2 surface fluxes at grid point scale estimated from a global 21 year reanalysis of atmospheric measurements, Journal of Geophysical Research-Atmospheres, 115, 10.1029/2010jd013887, 2010.

Connor, B. J., Boesch, H., Toon, G., Sen, B., Miller, C., and Crisp, D.: Orbiting carbon observatory: Inverse method and prospective error analysis, Journal of Geophysical Research-Atmospheres, 113, 10.1029/2006jd008336, 2008.

Conway, T. J., Tans, P. P., Waterman, L. S., and Thoning, K. W.: Evidence for interannual variability of the carbon cycle from the National Oceanic and Atmospheric Administration/Climate Monitoring and Diagnostics Laboratory Global Air Sampling Network, Journal of Geophysical Research-Atmospheres, 99, 22831-22855, 10.1029/94jd01951, 1994.

625 Crisp, D., Atlas, R. M., Breon, F. M., Brown, L. R., Burrows, J. P., Ciais, P., Connor, B. J., Doney, S. C., Fung, I. Y., Jacob, D. J., Miller, C. E., O'Brien, D., Pawson, S., Randerson, J. T., Rayner, P., Salawitch, R. J., Sander, S. P., Sen, B., Stephens, G. L., Tans, P. P., Toon, G. C., Wennberg, P. O., Wofsy, S. C., Yung, Y. L., Kuang, Z. M., Chudasama, B., Sprague, G., Weiss, B., Pollock, R., Kenyon, D., and Schroll, S.: The orbiting carbon observatory (OCO) mission, in: Trace Constituents in the Troposphere and Lower Stratosphere, edited by: Burrows, J. P., and Thompson, A. M., Advances in Space Research-Series, 4, 700-709, 10.1016/j.asr.2003.08.062, 2004.

Crisp, D., Fisher, B. M., O'Dell, C., Frankenberg, C., Basilio, R., Boesch, H., Brown, L. R., Castano, R., Connor, B., Deutscher, N. M.,
630 Eldering, A., Griffith, D., Gunson, M., Kuze, A., Mandrake, L., McDuffie, J., Messerschmidt, J., Miller, C. E., Morino, I., Natraj, V., Notholt, J., O'Brien, D. M., Oyafuso, F., Polonsky, I., Robinson, J., Salawitch, R., Sherlock, V., Smyth, M., Suto, H., Taylor, T. E., Thompson, D. R., Wennberg, P. O., Wunch, D., and Yung, Y. L.: The ACOS CO2 retrieval algorithm - Part II: Global X-CO2 data characterization, Atmospheric Measurement Techniques, 5, 687-707, 10.5194/amt-5-687-2012, 2012.

Crowell, S., Baker, D., Schuh, A., Basu, S., Jacobson, A. R., Chevallier, F., Liu, J. J., Deng, F., Feng, L., McKain, K., Chatterjee, A., Miller,
635 J. B., Stephens, B. B., Eldering, A., Crisp, D., Schimel, D., Nassar, R., O'Dell, C., Oda, T., Sweeney, C., Palmer, P. I., and Jones, D. B. A.: The 2015-2016 carbon cycle as seen from OCO-2 and the global in situ network, Atmospheric Chemistry and Physics, 19, 9797-9831, 10.5194/acp-19-9797-2019, 2019.

Deng, F., Chen, J. M., Ishizawa, M., Yuen, C.-W., Mo, G., Higuchi, K., Chan, D., and Maksyutov, S.: Global monthly CO2 flux inversion with a focus over North America, Tellus Series B-Chemical and Physical Meteorology, 59, 179-190, 10.1111/j.1600-0889.2006.00235.x,
640 2007.

Deng, F., Jones, D. B. A., Henze, D. K., Bousserez, N., Bowman, K. W., Fisher, J. B., Nassar, R., O'Dell, C., Wunch, D., Wennberg, P. O., Kort, E. A., Wofsy, S. C., Blumenstock, T., Deutscher, N. M., Griffith, D. W. T., Hase, F., Heikkinen, P., Sherlock, V., Strong, K., Sussmann, R., and Warneke, T.: Inferring regional sources and sinks of atmospheric CO2 from GOSAT XCO2 data, Atmospheric Chemistry and Physics, 14, 3703-3727, 10.5194/acp-14-3703-2014, 2014.

645 Ding, J., Chen, L., Ji, C., Hugelius, G., Li, Y., Liu, L., Qin, S., Zhang, B., Yang, G., Li, F., Fang, K., Chen, Y., Peng, Y., Zhao, X., He, H., Smith, P., Fang, J., and Yang, Y.: Decadal soil carbon accumulation across Tibetan permafrost regions, Nature Geoscience, 10, 420-+, 10.1038/ngeo2945, 2017.

Du, M., Li, Y., Zhang, F., Zhao, L., Li, H., Niu, B., He, Y., Zhang, X., Liu, J., Yonemura, S., and Tang, Y.: Recent changes of climate and livestock productions on the Tibetan Plateau and in situ observations of NEE, Journal of Arid Land Studies, 28, 139-142,
650 10.14976/jals.28.S_139, 2018.

Eldering, A., Wennberg, P. O., Crisp, D., Schimel, D. S., Gunson, M. R., Chatterjee, A., Liu, J., Schwandner, F. M., Sun, Y., O'Dell, C. W., Frankenberg, C., Taylor, T., Fisher, B., Osterman, G. B., Wunch, D., Hakkarainen, J., Tamminen, J., and Weir, B.: The Orbiting Carbon Observatory-2 early science investigations of regional carbon dioxide fluxes, Science, 358, 10.1126/science.aam5745, 2017.

Evensen, G.: Data Assimilation: The Ensemble Kalman Filter, 2, Springer-Verlag Berlin Heidelberg, 307 pp., 10.1007/978-3-642-03711-5,
655 2009.

Friedlingstein, P., O'Sullivan, M., Jones, M. W., Andrew, R. M., Hauck, J., Olsen, A., Peters, G. P., Peters, W., Pongratz, J., Sitch, S., Le Quere, C., Canadell, J. G., Ciais, P., Jackson, R. B., Alin, S., Aragao, L., Arneth, A., Arora, V., Bates, N. R., Becker, M., Benoit-Cattin, A., Bittig, H. C., Bopp, L., Bultan, S., Chandra, N., Chevallier, F., Chini, L. P., Evans, W., Florentie, L., Forster, P. M., Gasser, T., Gehlen, M., Gilfillan, D., Gkritzalis, T., Gregor, L., Gruber, N., Harris, I., Hartung, K., Haverd, V., Houghton, R. A., Ilyina, T., Jain, A. K., Joetzjer, E.,
660 Kadono, K., Kato, E., Kitidis, V., Korsbakken, J. I., Landschutzer, P., Lefevre, N., Lenton, A., Lienert, S., Liu, Z., Lombardozzi, D., Marland, G., Metzl, N., Munro, D. R., Nabel, J., Nakaoka, S. I., Niwa, Y., O'Brien, K., Ono, T., Palmer, P. I., Pierrot, D., Poulter, B., Resplandy, L., Robertson, E., Rodenbeck, C., Schwinger, J., Seferian, R., Skjelvan, I., Smith, A. J. P., Sutton, A. J., Tanhua, T., Tans, P. P., Tian, H., Tilbrook, B., Van der Werf, G., Vuichard, N., Walker, A. P., Wanninkhof, R., Watson, A. J., Willis, D., Wiltshire, A. J., Yuan, W. P., Yue, X., and Zaehle, S.: Global Carbon Budget 2020, Earth System Science Data, 12, 3269-3340, 10.5194/essd-12-3269-2020, 2020.

665 Ganjurjav, H., Hu, G., Wan, Y., Li, Y., Danjiu, L., and Gao, Q.: Different responses of ecosystem carbon exchange to warming in three types of alpine grassland on the central Qinghai-Tibetan Plateau, Ecology and Evolution, 8, 1507-1520, 10.1002/ece3.3741, 2018.

Gelaro, R., McCarty, W., Suárez, M. J., Todling, R., Molod, A., Takacs, L., Randles, C. A., Darmenov, A., Bosilovich, M. G., Reichle, R., Wargan, K., Coy, L., Cullather, R., Draper, C., Akella, S., Buchard, V., Conaty, A., da Silva, A. M., Gu, W., Kim, G.-K., Koster, R., Lucchesi, R., Merkova, D., Nielsen, J. E., Partyka, G., Pawson, S., Putman, W., Rienecker, M., Schubert, S. D., Sienkiewicz, M., and Zhao, B.: The
670 Modern-Era Retrospective Analysis for Research and Applications, Version 2 (MERRA-2), Journal of Climate, 30, 5419-5454, 10.1175/JCLI-D-16-0758.1, 2017.

Han, R. and Tian, X.: A dual-pass carbon cycle data assimilation system to estimate surface CO2 fluxes and 3D atmospheric CO2 concentrations from spaceborne measurements of atmospheric CO2, Geosci. Model Dev. Discuss., 2019, 1-29, 10.5194/gmd-2019-54, 2019.

Harris, N. L., Gibbs, D. A., Baccini, A., Birdsey, R. A., de Bruin, S., Farina, M., Fatoyinbo, L., Hansen, M. C., Herold, M., Houghton, R.
675 A., Potapov, P. V., Suarez, D. R., Roman-Cuesta, R. M., Saatchi, S. S., Slay, C. M., Turubanova, S. A., and Tyukavina, A.: Global maps of twenty-first century forest carbon fluxes, Nature Climate Change, 11, 10.1038/s41558-020-00976-6, 2021.

Hauck, J., Zeising, M., Le Quere, C., Gruber, N., Bakker, D. C. E., Bopp, L., Chau, T. T. T., Guerses, O., Ilyina, T., Landschuetzer, P., Lenton, A., Resplandy, L., Roedenbeck, C., Schwinger, J., and Seferian, R.: Consistency and Challenges in the Ocean Carbon Sink Estimate for the Global Carbon Budget, Frontiers in Marine Science, 7, 10.3389/fmars.2020.571720, 2020.

680 Hoesly, R. M., Smith, S. J., Feng, L., Klimont, Z., Janssens-Maenhout, G., Pitkanen, T., Seibert, J. J., Linh, V., Andres, R. J., Bolt, R. M., Bond, T. C., Dawidowski, L., Kholod, N., Kurokawa, J.-i., Li, M., Liu, L., Lu, Z., Moura, M. C. P., O'Rourke, P. R., and Zhang, Q.: Historical (1750-2014) anthropogenic emissions of reactive gases and aerosols from the Community Emissions Data System (CEDS), Geoscientific Model Development, 11, 369-408, 10.5194/gmd-11-369-2018, 2018.

Hopping, K. A., Knapp, A. K., Dorji, T., and Klein, J. A.: Warming and land use change concurrently erode ecosystem services in Tibet,
685 Global Change Biology, 24, 5534-5548, 10.1111/gcb.14417, 2018.

Jacobson, A. R., Schuldt, K. N., Miller, J. B., Oda, T., Tans, P., Arlyn, A., Mund, J., Ott, L., Collatz, G. J., Aalto, T., Afshar, S., Aikin, K., Aoki, S., Apadula, F., Baier, B., Bergamaschi, P., Beyersdorf, A., Biraud, S. C., Bollenbacher, A., Bowling, D., Brailsford, G., Abshire, J. B., Chen, G., Huilin, C., Lukasz, C., Sites, C., Colomb, A., Conil, S., Cox, A., Cristofanelli, P., Cuevas, E., Curcoll, R., Sloop, C. D., Davis, K., Wekker, S. D., Delmotte, M., DiGangi, J. P., Dlugokencky, E., Ehleringer, J., Elkins, J. W., Emmenegger, L., Fischer, M. L., Forster,
690 G., Frumau, A., Galkowski, M., Gatti, L. V., Gloor, E., Griffis, T., Hammer, S., Haszpra, L., Hatakka, J., Heliasz, M., Hensen, A., Hermanssen, O., Hintsa, E., Holst, J., Jaffe, D., Karion, A., Kawa, S. R., Keeling, R., Keronen, P., Kolari, P., Kominkova, K., Kort, E., Krummel, P., Kubistin, D., Labuschagne, C., Langenfelds, R., Laurent, O., Laurila, T., Lauvaux, T., Law, B., Lee, J., Lehner, I., Leuenberger, M., Levin, I., Levula, J., Lin, J., Lindauer, M., Loh, Z., Lopez, M., Luijkx, I. T., Myhre, C. L., Machida, T., Mammarella, I., Manca, G., Manning, A., Manning, A., Marek, M. V., Marklund, P., Martin, M. Y., Matsueda, H., McKain, K., Meijer, H., Meinhardt, F., Miles, N.,
695 Miller, C. E., Mölder, M., Montzka, S., Moore, F., Josep-Anton, M., Morimoto, S., Munger, B., Jaroslaw, N., Newman, S., Nichol, S., Niwa, Y., O'Doherty, S., Mikaell, O.-L., Paplawsky, B., Peischl, J., Peltola, O., Jean-Marc, P., Piper, S., Plass-Dölmer, C., Ramonet, M., Reyes-Sanchez, E., Richardson, S., Riris, H., Ryerson, T., Saito, K., Sargent, M., Sasakawa, M., Sawa, Y., Say, D., Scheeren, B., Schmidt, M., Schmidt, A., Schumacher, M., Shepson, P., Shook, M., Stanley, K., Steinbacher, M., Stephens, B., Sweeney, C., Thoning, K., Torn, M., Turnbull, J., Tørseth, K., Bulk, P. V. D., Dinther, D. V., Vermeulen, A., Viner, B., Vitkova, G., Walker, S., Weyrauch, D., Wofsy, S., Worthy,
700 D., Dickon, Y., and Miroslav, Z.: CarbonTracker CT2019B, 10.25925/20201008, 2020.

Jiang, F., Wang, H., Chen, J. M., Ju, W., Tian, X., Feng, S., Li, G., Chen, Z., Zhang, S., Lu, X., Liu, J., Wang, H., Wang, J., He, W., and Wu, M.: Regional CO2 fluxes from 2010 to 2015 inferred from GOSAT XCO2 retrievals using a new version of the Global Carbon Assimilation System, Atmospheric Chemistry and Physics, 21, 1963-1985, 10.5194/acp-21-1963-2021, 2021.

Jin, Z., Zhuang, Q., He, J.-S., Zhu, X., and Song, W.: Net exchanges of methane and carbon dioxide on the Qinghai-Tibetan Plateau from
705 1979 to 2100, Environmental Research Letters, 10, 10.1088/1748-9326/10/8/085007, 2015.

Jin, Z., Tian, X., Han, R., Fu, Y., Li, X., Mao, H., and Chen, C.: Tan-Tracker global daily NEE and ocean fluxes for 2015-2019 (TT2021 dataset) [dataset], 10.11888/Meteoro.tpdc.271317, 2021.

Kato, T., Tang, Y., Gu, S., Hirota, M., Du, M., Li, Y., and Zhao, X.: Temperature and biomass influences on interannual changes in CO2 exchange in an alpine meadow on the Qinghai-Tibetan Plateau, Global Change Biology, 12, 1285-1298, 10.1111/j.1365-2486.2006.01153.x,
710 2006.

Khatiwala, S., Tanhua, T., Fletcher, S. M., Gerber, M., Doney, S. C., Graven, H. D., Gruber, N., McKinley, G. A., Murata, A., Rios, A. F., and Sabine, C. L.: Global ocean storage of anthropogenic carbon, Biogeosciences, 10, 2169-2191, 10.5194/bg-10-2169-2013, 2013.

Kiel, M., O'Dell, C. W., Fisher, B., Eldering, A., Nassar, R., MacDonald, C. G., and Wennberg, P. O.: How bias correction goes wrong: measurement of X-CO2 affected by erroneous surface pressure estimates, Atmospheric Measurement Techniques, 12, 2241-2259,
715 10.5194/amt-12-2241-2019, 2019.

Lauvaux, T., Miles, N. L., Deng, A., Richardson, S. J., Cambaliza, M. O., Davis, K. J., Gaudet, B., Gurney, K. R., Huang, J., O'Keefe, D., Song, Y., Karion, A., Oda, T., Patarasuk, R., Razlivanov, I., Sarmiento, D., Shepson, P., Sweeney, C., Turnbull, J., and Wu, K.: High-resolution atmospheric inversion of urban CO2 emissions during the dormant season of the Indianapolis Flux Experiment (INFLUX), Journal of Geophysical Research-Atmospheres, 121, 5213-5236, 10.1002/2015jd024473, 2016.

720 Li, H., Zhang, F., Li, Y., Wang, J., Zhang, L., Zhao, L., Cao, G., Zhao, X., and Du, M.: Seasonal and inter-annual variations in CO2 fluxes over 10 years in an alpine shrubland on the Qinghai-Tibetan Plateau, China, Agricultural and Forest Meteorology, 228, 95-103, 10.1016/j.agrformet.2016.06.020, 2016.

Liang, A., Gong, W., Han, G., and Xiang, C.: Comparison of Satellite-Observed XCO2 from GOSAT, OCO-2, and Ground-Based TCCON, Remote Sensing, 9, 10.3390/rs9101033, 2017.

725 Liu, J., Bowman, K. W., Lee, M., Henze, D. K., Bousserez, N., Brix, H., Collatz, G. J., Menemenlis, D., Ott, L., Pawson, S., Jones, D., and Nassar, R.: Carbon monitoring system flux estimation and attribution: impact of ACOS-GOSAT X-CO2 sampling on the inference of terrestrial biospheric sources and sinks, Tellus Series B-Chemical and Physical Meteorology, 66, 10.3402/tellusb.v66.22486, 2014.

Liu, J., Baskaran, L., Bowman, K., Schimel, D., Bloom, A. A., Parazoo, N. C., Oda, T., Carroll, D., Menemenlis, D., Joiner, J., Commane, R., Daube, B., Gatti, L. V., McKain, K., Miller, J., Stephens, B. B., Sweeney, C., and Wofsy, S.: Carbon Monitoring System Flux Net
730 Biosphere Exchange 2020 (CMS-Flux NBE 2020), Earth System Science Data, 13, 299-330, 10.5194/essd-13-299-2021, 2021.

Marland, G.: Uncertainties in accounting for CO(2) from fossil fuels, Journal of Industrial Ecology, 12, 136-139, 10.1111/j.1530-9290.2008.00014.x, 2008.

McKinley, G. A., Fay, A. R., Lovenduski, N. S., and Pilcher, D. J.: Natural Variability and Anthropogenic Trends in the Ocean Carbon Sink, Annual Review of Marine Science, 9, 125-150, 10.1146/annurev-marine-010816-060529, 2017.

735 Nassar, R., Napier-Linton, L., Gurney, K. R., Andres, R. J., Oda, T., Vogel, F. R., and Deng, F.: Improving the temporal and spatial distribution of CO2 emissions from global fossil fuel emission data sets, Journal of Geophysical Research-Atmospheres, 118, 917-933, 10.1029/2012jd018196, 2013.

Nassar, R., Jones, D. B. A., Kulawik, S. S., Worden, J. R., Bowman, K. W., Andres, R. J., Suntharalingam, P., Chen, J. M., Brenninkmeijer, C. A. M., Schuck, T. J., Conway, T. J., and Worthy, D. E.: Inverse modeling of CO2 sources and sinks using satellite observations of CO2

740 from TES and surface flask measurements, Atmospheric Chemistry and Physics, 11, 6029-6047, 10.5194/acp-11-6029-2011, 2011.

Nassar, R., Jones, D. B. A., Suntharalingam, P., Chen, J. M., Andres, R. J., Wecht, K. J., Yantosca, R. M., Kulawik, S. S., Bowman, K. W., Worden, J. R., Machida, T., and Matsueda, H.: Modeling global atmospheric CO2 with improved emission inventories and CO2 production from the oxidation of other carbon species, Geoscientific Model Development, 3, 689-716, 10.5194/gmd-3-689-2010, 2010.

Nieberding, F., Wille, C., Fratini, G., Asmussen, M. O., Wang, Y., Ma, Y., and Sachs, T.: A long-term (2005-2019) eddy covariance data

745 set of CO2 and H2O fluxes from the Tibetan alpine steppe, Earth System Science Data, 12, 2505-2524, 10.5194/essd-12-2705-2020, 2020.

Niwa, Y. and Fujii, Y.: A conjugateBFGSmethod for accurate estimation of a posterior error covariance matrix in a linear inverse problem, Quarterly Journal of the Royal Meteorological Society, 146, 3118-3143, 10.1002/qj.3838, 2020.

O'Dell, C. W., Connor, B., Bösch, H., O'Brien, D., Frankenberg, C., Castano, R., Christi, M., Eldering, D., Fisher, B., Gunson, M., McDuffie, J., Miller, C. E., Natraj, V., Oyafuso, F., Polonsky, I., Smyth, M., Taylor, T., Toon, G. C., Wennberg, P. O., and Wunch, D.: The ACOS CO$_2$

750 retrieval algorithm – Part 1: Description and validation against synthetic observations, Atmospheric Measurement Techniques, 5, 99-121, 10.5194/amt-5-99-2012, 2012.

O'Dell, C. W., Eldering, A., Wennberg, P. O., Crisp, D., Gunson, M. R., Fisher, B., Frankenberg, C., Kiel, M., Lindqvist, H., Mandrake, L., Merrelli, A., Natraj, V., Nelson, R. R., Osterman, G. B., Payne, V. H., Taylor, T. E., Wunch, D., Drouin, B. J., Oyafuso, F., Chang, A., McDuffie, J., Smyth, M., Baker, D. F., Basu, S., Chevallier, F., Crowell, S. M. R., Feng, L., Palmer, P. I., Dubey, M., García, O. E., Griffith,

755 D. W. T., Hase, F., Iraci, L. T., Kivi, R., Morino, I., Notholt, J., Ohyama, H., Petri, C., Roehl, C. M., Sha, M. K., Strong, K., Sussmann, R., Te, Y., Uchino, O., and Velazco, V. A.: Improved retrievals of carbon dioxide from Orbiting Carbon Observatory-2 with the version 8 ACOS algorithm, Atmospheric Measurement Techniques, 11, 6539-6576, 10.5194/amt-11-6539-2018, 2018.

Oda, T. and Maksyutov, S.: A very high-resolution (1 km×1 km) global fossil fuel CO2 emission inventory derived using a point source database and satellite observations of nighttime lights, Atmos. Chem. Phys., 11, 543-556, 10.5194/acp-11-543-2011, 2011.

760 Oda, T., Maksyutov, S., and Andres, R. J.: The Open-source Data Inventory for Anthropogenic CO2, version 2016 (ODIAC2016): a global monthly fossil fuel CO2 gridded emissions data product for tracer transport simulations and surface flux inversions, Earth System Science Data, 10, 87-107, 10.5194/essd-10-87-2018, 2018a.

Oda, T., Maksyutov, S., and Andres, R. J.: The Open-source Data Inventory for Anthropogenic CO2, version 2016 (ODIAC2016): a global monthly fossil fuel CO2 gridded emissions data product for tracer transport simulations and surface flux inversions, Earth Syst. Sci. Data,

765 10, 87-107, 10.5194/essd-10-87-2018, 2018b.

Olsen, S. C., Wuebbles, D. J., and Owen, B.: Comparison of global 3-D aviation emissions datasets, Atmospheric Chemistry and Physics, 13, 429-441, 10.5194/acp-13-429-2013, 2013.

Peters, W., Jacobson, A. R., Sweeney, C., Andrews, A. E., Conway, T. J., Masarie, K., Miller, J. B., Bruhwiler, L. M. P., Petron, G., Hirsch, A. I., Worthy, D. E. J., van der Werf, G. R., Randerson, J. T., Wennberg, P. O., Krol, M. C., and Tans, P. P.: An atmospheric perspective on

770 North American carbon dioxide exchange: CarbonTracker, Proceedings of the National Academy of Sciences of the United States of America, 104, 18925-18930, 10.1073/pnas.0708986104, 2007.

Peylin, P., Law, R. M., Gurney, K. R., Chevallier, F., Jacobson, A. R., Maki, T., Niwa, Y., Patra, P. K., Peters, W., Rayner, P. J., Roedenbeck, C., van der Laan-Luijkx, I. T., and Zhang, X.: Global atmospheric carbon budget: results from an ensemble of atmospheric CO2 inversions, Biogeosciences, 10, 6699-6720, 10.5194/bg-10-6699-2013, 2013.

775 Piao, S., Fang, J., Ciais, P., Peylin, P., Huang, Y., Sitch, S., and Wang, T.: The carbon balance of terrestrial ecosystems in China, Nature, 458, 1009-U1082, 10.1038/nature07944, 2009.

Piao, S., Zhang, X., Wang, T., Liang, E., Wang, S., Zhu, J., and Niu, B.: Responses and feedback of the Tibetan Plateau's alpine ecosystem to climate change, Chinese Science Bulletin, 64, 2842-2855, 2019.

Piao, S., Wang, X., Wang, K., Li, X., Bastos, A., Canadell, J. G., Ciais, P., Friedlingstein, P., and Sitch, S.: Interannual variation of terrestrial

780 carbon cycle: Issues and perspectives, Global Change Biology, 26, 300-318, 10.1111/gcb.14884, 2020.

Qiu, J.: The third pole, Nature, 454, 393-396, 10.1038/454393a, 2008.

Randerson, J. T., Van Der Werf, G. R., Giglio, L., Collatz, G. J., and Kasibhatla, P. S.: Global Fire Emissions Database, Version 4.1 (GFEDv4), 10.3334/ORNLDAAC/1293, 2017.

Rödenbeck, C.: Estimating CO2 sources and sinks from atmospheric mixing ratio measurements using a global inversion of atmospheric

785 transport, Technical reports, 2005, 2005.

Simone, N., Stettler, M., Eastham, S., and Barrett, S.: Aviation Emissions Inventory Code (AEIC) User Manual (R1), Laboratory for Aviation and the Environment, Massachusetts Institute of TechnologyLAE-2013-001-N, 2013.

Suntharalingam, P., Jacob, D. J., Palmer, P. I., Logan, J. A., Yantosca, R. M., Xiao, Y. P., Evans, M. J., Streets, D. G., Vay, S. L., and Sachse, G. W.: Improved quantification of Chinese carbon fluxes using CO2/CO correlations in Asian outflow, Journal of Geophysical Research-Atmospheres, 109, 10.1029/2003jd004362, 2004.

Takagi, H., Saeki, T., Oda, T., Saito, M., Valsala, V., Belikov, D., Saito, R., Yoshida, Y., Morino, I., Uchino, O., Andres, R. J., Yokota, T., and Maksyutov, S.: On the Benefit of GOSAT Observations to the Estimation of Regional CO2 Fluxes, Sola, 7, 161-164, 10.2151/sola.2011-041, 2011.

Takahashi, T., Sutherland, S. C., Sweeney, C., Poisson, A., Metzl, N., Tilbrook, B., Bates, N., Wanninkhof, R., Feely, R. A., Sabine, C., Olafsson, J., and Nojiri, Y.: Global sea-air CO2 flux based on climatological surface ocean pCO(2), and seasonal biological and temperature effects, Deep-Sea Research Part Ii-Topical Studies in Oceanography, 49, 1601-1622, 10.1016/s0967-0645(02)00003-6, 2002.

Takahashi, T., Sutherland, S. C., Wanninkhof, R., Sweeney, C., Feely, R. A., Chipman, D. W., Hales, B., Friederich, G., Chavez, F., Sabine, C., Watson, A., Bakker, D. C. E., Schuster, U., Metzl, N., Yoshikawa-Inoue, H., Ishii, M., Midorikawa, T., Nojiri, Y., Koertzinger, A., Steinhoff, T., Hoppema, M., Olafsson, J., Arnarson, T. S., Tilbrook, B., Johannessen, T., Olsen, A., Bellerby, R., Wong, C. S., Delille, B., Bates, N. R., and de Baar, H. J. W.: Climatological mean and decadal change in surface ocean pCO(2), and net sea-air CO2 flux over the global oceans, Deep-Sea Research Part Ii-Topical Studies in Oceanography, 56, 554-577, 10.1016/j.dsr2.2008.12.009, 2009.

Tian, X. and Feng, X.: A non-linear least squares enhanced POD-4DVar algorithm for data assimilation, Tellus A: Dynamic Meteorology and Oceanography, 67, 10.3402/tellusa.v67.25340, 2015.

Tian, X., Han, R., and Zhang, H.: An Adjoint-Free Alternating Direction Method for Four-Dimensional Variational Data Assimilation With Multiple Parameter Tikhonov Regularization, Earth and Space Science, 7, 10.1029/2020ea001307, 2020.

Tian, X., Zhang, H., Feng, X., and Xie, Y.: Nonlinear least squares En4DVar to 4DEnVar methods for data assimilation: formulation, analysis, and preliminary evaluation, Monthly Weather Review, 146, 77-93, 10.1175/mwr-d-17-0050.1, 2018.

Tian, X., Xie, Z., Cai, Z., Liu, Y., Fu, Y., and Zhang, H.: The Chinese carbon cycle data-assimilation system (Tan-Tracker), Chinese Science Bulletin, 59, 1541-1546, 10.1007/s11434-014-0238-1, 2014a.

Tian, X., Xie, Z., Liu, Y., Cai, Z., Fu, Y., Zhang, H., and Feng, L.: A joint data assimilation system (Tan-Tracker) to simultaneously estimate surface CO2 fluxes and 3-D atmospheric CO2 concentrations from observations, Atmospheric Chemistry and Physics, 14, 13281-13293, 10.5194/acp-14-13281-2014, 2014b.

van der Werf, G. R., Randerson, J. T., Giglio, L., van Leeuwen, T. T., Chen, Y., Rogers, B. M., Mu, M., van Marle, M. J. E., Morton, D. C., Collatz, G. J., Yokelson, R. J., and Kasibhatla, P. S.: Global fire emissions estimates during 1997–2016, Earth Syst. Sci. Data, 9, 697-720, 10.5194/essd-9-697-2017, 2017.

Villalobos, Y., Rayner, P., Thomas, S., and Silver, J.: The potential of Orbiting Carbon Observatory-2 data to reduce the uncertainties in CO2 surface fluxes over Australia using a variational assimilation scheme, Atmospheric Chemistry and Physics, 20, 8473-8500, 10.5194/acp-20-8473-2020, 2020.

Wang, H., Jiang, F., Wang, J., Ju, W., and Chen, J. M.: Terrestrial ecosystem carbon flux estimated using GOSAT and OCO-2 XCO2 retrievals, Atmospheric Chemistry and Physics, 19, 12067-12082, 10.5194/acp-19-12067-2019, 2019.

Watson, A. J., Schuster, U., Shutler, J. D., Holding, T., Ashton, I. G. C., Landschuetzer, P., Woolf, D. K., and Goddijn-Murphy, L.: Revised estimates of ocean-atmosphere CO2 flux are consistent with ocean carbon inventory, Nature Communications, 11, 10.1038/s41467-020-18203-3, 2020.

Wu, M., Scholze, M., Kaminski, T., Vossbeck, M., and Tagesson, T.: Using SMOS soil moisture data combining CO2 flask samples to constrain carbon fluxes during 2010-2015 within a Carbon Cycle Data Assimilation System (CCDAS), Remote Sensing of Environment, 240, 10.1016/j.rse.2020.111719, 2020.

Wunch, D., Toon, G. C., Sherlock, V., Deutscher, N. M., Liu, X., Feist, D. G., and Wennberg, P. O.: The Total Carbon Column Observing Network's GGG2014 Data Version [dataset], doi:10.14291/tccon.ggg2014.documentation.R0/1221662, 2015.

Wunch, D., Toon, G. C., Blavier, J. F. L., Washenfelder, R. A., Notholt, J., Connor, B. J., Griffith, D. W. T., Sherlock, V., and Wennberg, P. O.: The Total Carbon Column Observing Network, Philos T R Soc A, 369, 2087-2112, 10.1098/rsta.2010.0240, 2011.

Wunch, D., Wennberg, P. O., Osterman, G., Fisher, B., Naylor, B., Roehl, C. M., O'Dell, C., Mandrake, L., Viatte, C., Kiel, M., Griffith, D. W. T., Deutscher, N. M., and Velazco, V. A.: Comparisons of the Orbiting Carbon Observatory-2 (OCO-2) XCO2 measurements with TCCON, Atmospheric Measurement Techniques, 10, 2209-2238, 10.5194/amt-10-2209-2017, 2017.

Yao, T., Xue, Y., Chen, D., Chen, F., Thompson, L., Cui, P., Koike, T., Lau, W. K. M., Lettenmaier, D., Mosbrugger, V., Zhang, R., Xu, B., Dozier, J., Gillespie, T., Gu, Y., Kang, S., Piao, S., Sugimoto, S., Ueno, K., Wang, L., Wang, W., Zhang, F., Sheng, Y., Guo, W., Ailikun, Yang, X., Ma, Y., Shen, S. S. P., Su, Z., Chen, F., Liang, S., Liu, Y., Singh, V. P., Yang, K., Yang, D., Zhao, X., Qian, Y., Zhang, Y., and Li, Q.: Recent Third Pole's Rapid Warming Accompanies Cryospheric Melt and Water Cycle Intensification and Interactions between Monsoon and Environment: Multidisciplinary Approach with Observations, Modeling, and Analysis, Bulletin of the American Meteorological Society, 100, 423-444, 10.1175/bams-d-17-0057.1, 2019.

Yevich, R. and Logan, J. A.: An assessment of biofuel use and burning of agricultural waste in the developing world, Global Biogeochemical Cycles, 17, 10.1029/2002gb001952, 2003.

Yokota, T., Yoshida, Y., Eguchi, N., Ota, Y., Tanaka, T., Watanabe, H., and Maksyutov, S.: Global Concentrations of CO2 and CH4 Retrieved from GOSAT: First Preliminary Results, Sola, 5, 160-163, 10.2151/sola.2009-041, 2009.

845 Zhang, H. and Tian, X.: An Efficient Local Correlation Matrix Decomposition Approach for the Localization Implementation of Ensemble-Based Assimilation Methods, Journal of Geophysical Research-Atmospheres, 123, 3556-3573, 10.1002/2017jd027999, 2018.

Zscheischler, J., Mahecha, M. D., Avitabile, V., Calle, L., Carvalhais, N., Ciais, P., Gans, F., Gruber, N., Hartmann, J., Herold, M., Ichii, K., Jung, M., Landschutzer, P., Laruelle, G. G., Lauerwald, R., Papale, D., Peylin, P., Poulter, B., Ray, D., Regnier, P., Rodenbeck, C., Roman-Cuesta, R. M., Schwalm, C., Tramontana, G., Tyukavina, A., Valentini, R., van der Werf, G., West, T. O., Wolf, J. E., and Reichstein, M.: Reviews and syntheses: An empirical spatiotemporal description of the global surface-atmosphere carbon fluxes: opportunities and data 850 limitations, Biogeosciences, 14, 3685-3703, 10.5194/bg-14-3685-2017, 2017.